Pressure Fluctuations induced by a Hypersonic Turbulent Boundary Layer

LIAN DUAN[1], MEELAN M. CHOUDHARI[2]
AND CHAO ZHANG[1]

[1]Missouri University of Science and Technology, MO 65409, USA
[2]NASA Langley Research Center, Hampton, VA 23681, USA

Direct numerical simulations (DNS) are used to examine the pressure fluctuations generated by a spatially-developed Mach 5.86 turbulent boundary layer. The unsteady pressure field is analyzed at multiple wall-normal locations, including those at the wall, within the boundary layer (including inner layer, the log layer, and the outer layer), and in the free stream. The statistical and structural variations of pressure fluctuations as a function of wall-normal distance are highlighted. Computational predictions for mean velocity profiles and surface pressure spectrum are in good agreement with experimental measurements, providing a first ever comparison of this type at hypersonic Mach numbers. The simulation shows that the dominant frequency of boundary-layer-induced pressure fluctuations shifts to lower frequencies as the location of interest moves away from the wall. The pressure wave propagates with a speed nearly equal to the local mean velocity within the boundary layer (except in the immediate vicinity of the wall) while the propagation speed deviates from the Taylor's hypothesis in the free stream. Compared with the surface pressure fluctuations, which are primarily vortical, the acoustic pressure fluctuations in the free stream exhibit a significantly lower dominant frequency, a greater spatial extent, and a smaller bulk propagation speed. The freestream pressure structures are found to have similar Lagrangian time and spatial scales as the acoustic sources near the wall. As the Mach number increases, the freestream acoustic fluctuations exhibit increased radiation intensity, enhanced energy content at high frequencies, shallower orientation of wave fronts with respect to the flow direction, and larger propagation velocity.

1. Introduction

Understanding the physics of the pressure fluctuations induced by high-speed turbulent boundary layers are of major theoretical and practical importance. From a practical point of view, the fluctuating pressure on aerodynamic surfaces of flight vehicles plays an important role in vibrational loading and often leads to damaging effects as fatigue and flutter (Willmarth 1975; Blake 1986; Bull 1996). The freestream pressure fluctuations radiated from the turbulent boundary layer on the nozzle wall in a conventional hypersonic wind tunnel is largely responsible for the genesis of tunnel background disturbances (commonly referred to as tunnel noise) (Laufer 1964; Stainback 1971; Pate 1978). Such facility disturbances significantly impact laminar-turbulent transition behavior of the test article, leading to an earlier onset of transition relative to that in a flight environment or in a quiet tunnel (Schneider 2001). An in-depth knowledge of the nature

of pressure fluctuations in the high-speed regime is essential to the structural design of launch vehicles and to enabling a better use of transition data from the noisy hypersonic facilities. From a theoretical point of view, a better understanding of the pressure fluctuations could lead to a better understanding of the vorticity dynamics in the boundary layer since high-vorticity regions are strongly correlated with low-pressure regions (Kim 1989; Kida & Miura 1998; Cadot *et al.* 1995). Moreover, pressure fluctuations are an important ingredient in turbulence as they appear in statistical correlations such as the pressure-strain correlation terms which redistribute turbulence among different components of fluctuating velocity. The modeling of the pressure-strain terms in the transport equations for the Reynolds stresses and the dissipation tensor is regarded as one of the major issues in the Reynolds stress closure.

The analysis of the pressure fluctuations in the context of incompressible boundary layers is based on the Poisson equation. The source term in the Poisson equation is composed of two parts that generate, respectively, what are commonly referred to as the rapid (linear) and slow (nonlinear) parts of the pressure fluctuation field. Examples of existing studies of global pressure field induced by incompressible boundary layers include those by Kim (1989); Tsuji *et al.* (2007, 2012); Kat & Oudheusden (2012); Naka *et al.* (2015) among many others. The pressure fluctuations induced by a high-speed turbulent boundary layer are, however, fundamentally more complicated than the low-speed counterpart. At high speeds, pressure fluctuations of acoustic mode emerge in the form of eddy Mach waves. The pressure fluctuations in a turbulent boundary layer thus include contributions from both vorticity and acoustic modes. The former component is typically dominant within the boundary layer while the latter is dominant in the free stream. The relative importance of the two modes in different regions of the boundary layer at high speeds is largely unknown and a detailed analysis of the turbulent correlations containing pressure fluctuations is lacking.

Although there is a significant amount of literature on the behavior, distribution, and scaling of velocity fluctuations in high-speed turbulent boundary layers (Smits & Dussauge 2006), the corresponding behavior of pressure fluctuations is much less known. No measurement technique so far has been able to globally measure the pressure fluctuations inside the boundary layer. Thus existing measurements of pressure fluctuations due to high-speed turbulent boundary layers consist largely of those at the surface using surface-mounted pressure transducers. The few existing measurements of fluctuating wall pressure signals beneath supersonic turbulent boundary layers include early measurements by Kistler & Chen (1963) and by Maestrello (1969) for boundary layers with M_∞ ranging from 1.33 to 5, and more recently by Beresh *et al.* (2011) for boundary layers with M_∞ up to 3. These measurements exhibit a considerable degree of scatter. For example, the measurements by Kistler & Chen (1963) and by Maestrello (1969) found discrepancies in the magnitude of wall pressure fluctuations as large as 30%. The recent data acquired by Beresh *et al.* (2011) showed similar large scatter across a broad compilation of high-speed measurements. As pointed out by several authors (Dolling & Dussauge 1989; Beresh *et al.* 2011), there are few (if any) reliable measurements of the variance of the wall pressure fluctuations and its frequency spectra, due to the poor spatial resolution of pressure transducers or limitations in the frequency response of pressure sensors. Previous DNS studies of pressure fluctuations induced by high-speed boundary layers focused on the wall pressure and were limited to moderate freestream Mach numbers (up to Mach 4) (Bernardini & Pirozzoli 2011; Marco *et al.* 2013). To the knowledge of the authors, no data exist for turbulent boundary layers in the hypersonic regime that provide global access to the fluctuating pressure field.

As far as the freestream acoustic pressure fluctuations are concerned, the body of avail-

able data is even more scarce. Although a number of investigators have reported measurements of freestream disturbance intensity in high-speed facilities at both supersonic and hypersonic Mach numbers (Donaldson & Coulter 1995; Bounitch *et al.* 2011; Masutti *et al.* 2012), the measurements by Laufer (1964) still provide one of the few datasets that are detailed enough to be suitable for comparison or model development. Similar to the wall-pressure measurements, Laufer's measurements of the acoustic fluctuations in the freestream region (Laufer 1964) are subject to analogous sources of experimental error. Moreover, as noted by Laufer, the interpretation of disturbance measurements in a wind tunnel is further complicated by the fact that the measurements reflect the combined outcome of acoustic radiation from all sides of the tunnel wall. As a result, highly accurate measurements of the absolute amplitudes of the radiated acoustic energy were not pursued during his experiments and only the statistical quantities that were least likely to be influenced by the presence of multiple tunnel walls were investigated.

Direct numerical simulation (DNS) is a valuable tool that can overcome some of the aforementioned difficulties with experimental measurements and, hence, provide access to the global fluctuating pressure field that is difficult to obtain otherwise. For the study of the freestream pressure field, in particular, DNS has the additional benefit of easily isolating the acoustic radiation from a single surface as against the typical case of multiple tunnel walls in an experiment. Successful applications of DNS for studying acoustic radiation from turbulent boundary layers at subsonic and supersonic Mach numbers have been reported by Gloerfelt & Berland (2013) (Mach 0.5) and by Duan *et al.* (2014) (Mach 2.5), respectively.

The objective of the current paper is to document the statistical and structural variation of boundary-layer-induced pressure fluctuations as a function of wall-normal distance. The database to be used is obtained from a direct numerical simulation of a spatially-developing, flat-plate, nominally Mach 6 turbulent boundary layer, with the freestream and wall-temperature conditions representative of those at the nozzle exit of the Purdue Mach 6 Quiet Tunnel under noisy operations (Schneider 2008; Steen 2010). The physical realism and accuracy of the computed flow fields are first established by comparing with existing experimental results. Given that the DNS grids are designed to adequately capture both the the boundary layer and the near field of acoustic fluctuations radiated by the boundary layer, the present study is the first attempt, as far as we know, to investigate the detailed pressure statistics induced by a hypersonic turbulent boundary layer that includes the radiated pressure fluctuations in the near field, in addition to those generated within the boundary layer. To our knowledge, except the study by Duan *et al.* (2014), all previous DNS studies of supersonic turbulent boundary layers have focused exclusively on flow features within the boundary layer. The characteristics associated with the primarily vortical pressure signal within the boundary layer and the acoustic pressure signal in the free stream are compared.

The remaining part of this paper is structured as follows. The flow conditions selected for numerical simulation and the numerical method used are outlined in section 2. Section 3 is focused on the analysis of statistical and structural variations of pressure fluctuations as a function of wall-normal distance. The various statistics examined include pressure fluctuation intensities, power spectral densities, two-point pressure correlations, and propagation speeds. Section 4 discusses the characteristics of freestream acoustic radiation, including modal analysis, wave-front orientation, and acoustic sources contributing to the acoustic radiation in the free stream. Conclusions from the study are presented in section 5.

M_∞	U_∞(m/s)	ρ_∞(kg/m^3)	T_∞(K)
5.86	870.4	0.0427	54.97

Table 1: Freestream conditions for Mach 6 DNS of turbulent boundary layers.

2. Simulation details

Table 1 outlines the freestream flow condition for the present simulations including the freestream Mach number M_∞, density ρ_∞, temperature T_∞. The mean surface temperature T_w is assumed to be equal to $T_w/T_r = 0.76$, with the recovery temperature T_r estimated based on a recovery factor of 0.89. Throughout this paper, subscripts ∞ and w will be used to denote quantities at the boundary layer edge and at the wall, respectively. The freestream condition is selected to be similar to the conditions of the Boeing/AFOSR Mach-6 Quiet Tunnel (Schneider 2001; Steen 2010) (BAM6QT) under noisy operations, so that one-to-one comparison between DNS and experimental results can be conducted to establish the physical realism and accuracy of the computed flow fields.

2.1. *Governing equations and numerical methods*

The details of the DNS methodology, including numerical methods, initial and boundary conditions, have been documented in our previous paper (Duan *et al.* 2014). Therefore, only a cursory description is given here.

The full three-dimensional compressible Navier-Stokes equations in conservation form are solved in generalized curvilinear coordinates. The working fluid is assumed to be a perfect gas and the usual constitutive relations for a Newtonian fluid are used: the viscous stress tensor is linearly related to the rate-of-strain tensor, and the heat flux vector is linearly related to the temperature gradient through the Fourier's law. The coefficient of viscosity μ is computed from the Sutherlands's law, and the coefficient of thermal conductivity κ is computed from $\kappa = \mu C_p/Pr$, with the molecular Prandtl number $Pr = 0.71$.

A 7th-order weighted essentially non-oscillatory (WENO) scheme is used to compute the convective flux terms. Compared with the original finite-difference WENO introduced by Jiang & Shu (1996), the present WENO scheme is optimized by means of limiters (Taylor *et al.* 2006; Wu & Martín 2007) to reduce the numerical dissipation. For the viscous flux terms, a 4th order central difference scheme is used. The 3rd order low storage Runge-Kutta scheme by Williamson (1980) is used for time integration. The DNS code has been extensively validated in previous work for simulating supersonic and hypersonic turbulent boundary layers (Martín 2007; Wu & Martín 2007, 2008; Duan *et al.* 2010, 2011; Duan & Martín 2011; Priebe & Martín 2012). The optimized WENO has been shown to be adequate for time-accurate simulations of compressible turbulence (Martín 2007; Wu & Martín 2007, 2008; Duan *et al.* 2010, 2011; Duan & Martín 2011; Priebe & Martín 2012). The shock-capturing capability of the algorithm guarantees numerical stability and robustness under the present high-Mach-number condition.

2.2. *Computational domain and simulation setup*

Figure 1 shows a general computational set-up for the DNS in the present work, which parallels the setup in Duan *et al.* (2014) for the Mach 2.5 simulation, wherein the effects of domain size and grid resolution were also assessed. The choice of grid parameters for the present study is based on lessons learned from Duan *et al.* (2014) as summarized
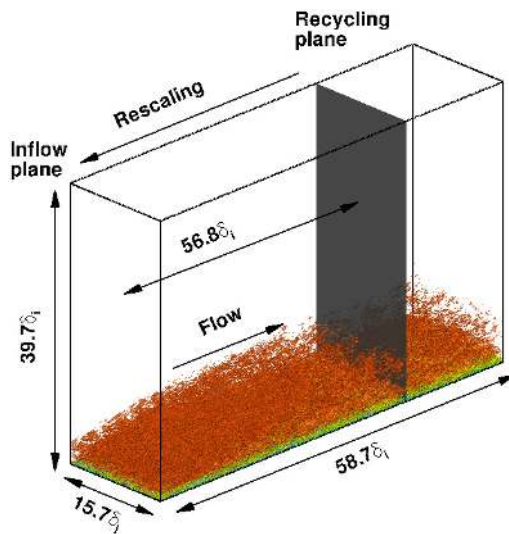
Figure 1: Computational domain and simulation setup for baseline DNS case. The reference length δ_i is the thickness of the boundary layer (based on 99% of the freestream velocity) at the inlet plane. An instantaneous flow is shown in the domain, visualized by iso-surface of the magnitude of density gradient, $|\nabla \rho| \delta_i / \rho_\infty = 0.9825$, colored by the streamwise velocity component (with levels from 0 to U_∞, blue to red). x, y, and z are, respectively, the streamwise, spanwise, and wall-normal coordinates.

in table 2. The streamwise domain length (L_x) is selected to be larger than the eddy decorrelation distance to guarantee minimal spurious correlation being introduced due to the inflow turbulence generation. The spanwise domain (L_y) is chosen based on monitoring the decay in cross-correlation of pressure fluctuation as a function of spanwise separation. Uniform grid spacings are used in the streamwise and spanwise directions with grid spacings. The grids in the wall-normal direction are clustered in the boundary layer with $\Delta z^+ \approx 0.5$ at the wall, and kept uniform with $\Delta z^+ \approx 5$ in the freestream until up to approximately $5.5\delta_i$ or 3.2δ (figure 2), where δ_i and δ represent the mean boundary layer thickness based on $u/U_\infty = 0.99$ at the inflow boundary and at the downstream location selected for statistical analysis ($x_a = 54.1\delta_i$), respectively. Such wall-normal grids are designed to adequately resolve both the boundary layer and the near field of acoustic fluctuations radiated by the boundary layer. The '+' superscript denotes non-dimensionalization by the viscous length scale $z_\tau = \nu_w / u_\tau$, where ν_w is the kinematic viscosity at the wall and $u_\tau = \sqrt{\tau_w / \rho_w}$ is the friction velocity (τ_w is the wall-shear stress and ρ_w is the density at the wall). Unless otherwise stated, the grid resolutions given in this section are normalized by the viscous length scale z_τ at the selected downstream location x_a. Analysis of the simulation database has also shown that the Kolmogorov length scale at x_a is comparable with the local viscous length.

The turbulent inflow is generated using the recycling/rescaling method developed by Xu & Martín (2004) with the recycling station set at $56.7\delta_i$ downstream of the inlet. The selected rescaling length is similar to the range of the optimum recycling length of approximately $30\delta_i$ to $99\delta_i$ as suggested by Simens et al. (2009) to accommodate the eddy decorrelation length and to minimize inlet transient as a result of the recycling process. The original rescaling method is modified by adding the dynamic translation operations (Morgan et al. 2011) to improve low-frequency characteristics of the gener-
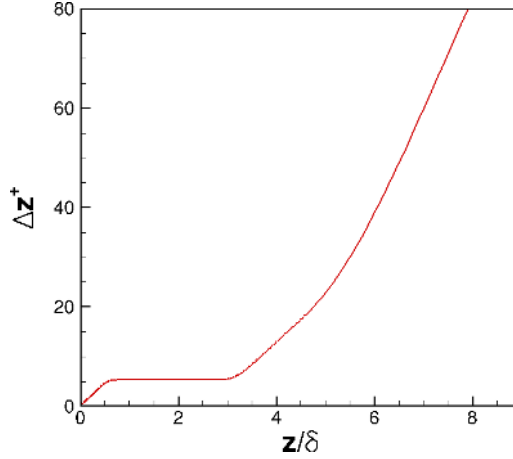
Figure 2: The wall-normal grid distribution. The grid spacing Δz^+ is normalized by the viscous length scale at the selected downstream location for statistical analysis ($x_a = 54.1\delta_i$).

$N_x \times N_y \times N_z$	L_x/δ_i	L_y/δ_i	L_z/δ_i	Δx^+	Δy^+	Δz^+_{min}	Δz^+_{max}
$1600 \times 800 \times 500$	58.7	15.7	39.7	9.63	5.14	0.51	5.33

Table 2: Grid resolution and domain size for the direct numerical simulation. L_x, L_y, and L_z are the domain size in the streamwise, spanwise, and wall-normal directions, respectively. Δx^+ and Δy^+ are the uniform grid spacing in the streamwise and spanwise directions, respectively. Δz^+_{min} and Δz^+_{max} are the minimum and maximum wall-normal grid spacing for $0 \leqslant z/\delta_i \leqslant 5.5$. The grid spacings are reported in terms of the viscous length scale z_τ evaluated at the station selected for statistical analysis $x_a/\delta_i = 54.1$. $\delta_i = 13.8$ mm.

ated inflow turbulence and by including a freestream filter to remove artificial freestream acoustics at the inlet of the computational domain introduced due to the coupling between the recycling and inflow plane (Duan *et al.* 2014). This removal of recycled fluctuations in the free stream ensures that the freestream acoustic disturbances within the domain are radiated entirely from the boundary-layer turbulence rather than convected downstream from the artificial inflow. In addition, numerical experiments have been conducted with varying filter type and filtering location to ensure that the freestream filtering has negligible effects on the pressure statistics at the selected downstream location for statistical analysis ($x_a = 54.1\delta_i$).

On the wall, no-slip conditions are applied for the three velocity components and an isothermal condition is used for the temperature with $T_w \approx 0.76T_r$. The density is computed from the continuity equation. At the top and outlet boundaries, unsteady non-reflecting boundary conditions based on Thompson (1987) are imposed. Periodic boundary conditions are used in the spanwise direction.

For the current spatial simulations, the boundary layer grows slowly in the streamwise direction, with both the boundary-layer thickness δ and the displacement thickness δ^* increase by a factor of approximately two across the length of the simulation domain (figure 3). Correspondingly, the Karman number Re_τ increases from approximately 200
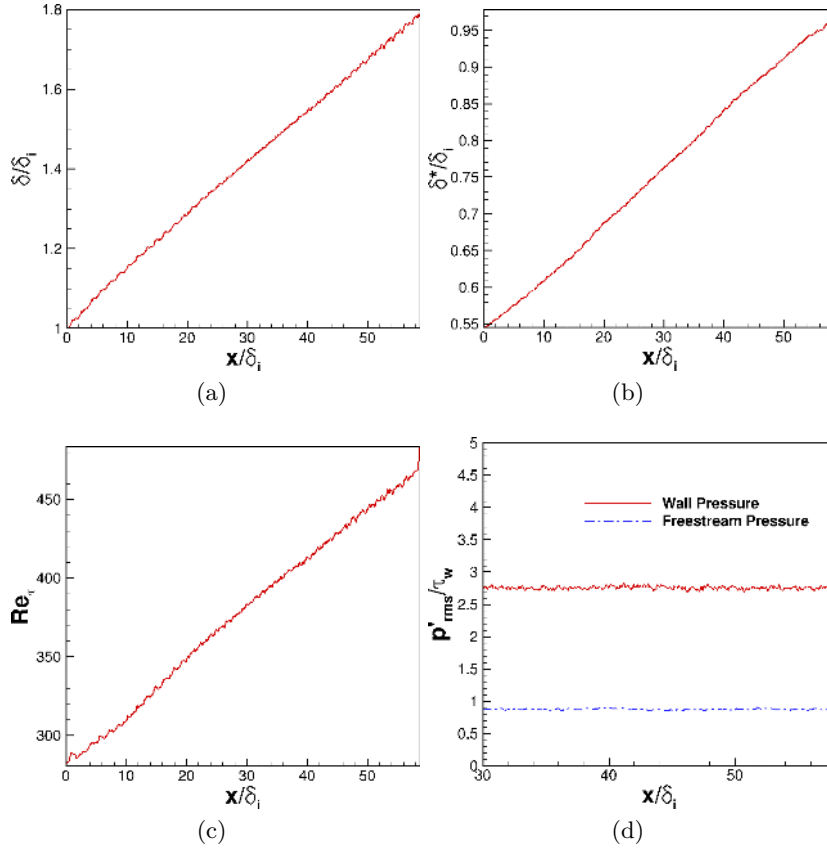
Figure 3: Evolution of boundary-layer parameters with streamwise distance. (a) δ/δ_i; (b) δ^*/δ_i; (c) Re_τ; (d) p'_{rms}/τ_w at $z/\delta_i = 0$ and 4.5.

at the inlet to 500 at the outlet with a useful range of $Re_\tau = 350 - 460$ where the boundary layer has recovered from the initial transient due to the recycling method. The stremwise computational domain is large enough for the memory of the inflow generation to fade out and a nearly uniform acoustic radiation field to be established. In particular, figure 3d shows that the pressure fluctuations at the wall and in the freestream have become nearly homogeneous in the streamwise direction after $x/\delta_i \approx 30$.

In the following section, averages are first calculated over a streamwise window of $[x_a - 0.9\delta_i, x_a + 0.9\delta_i]$ ($x_a = 54.1\delta_i$) and spanwise locations for each instantaneous flow field; then, an ensemble average over 153 flow field snapshots spanning a time interval of approximately $240\delta_i/U_\infty$ (corresponding to $12.5\delta_i/u_\tau$) is calculated. To monitor the statistical convergence, flow statistics are computed by averaging over the whole or half the number of the flow-field snapshots and negligible difference ($< 1\%$) is observed between the two.

Power spectra are calculated using the Welch method (Welch 1967) with eight segments and 50% overlap. A Hamming window is used for weighting the data prior to the fast Fourier transform (FFT) processing. The sampling frequency is approximately $63U_\infty/\delta_i$, or 4 MHz, and the length of an individual segment is approximately $53.2\delta_i/U_\infty$.

$T_w(k)$	T_w/T_r	Re_θ	Re_τ	$Re_{\delta2}$	$\theta(\text{mm})$	H	$\delta(\text{mm})$	$z_\tau(\mu\text{m})$	$u_\tau(\text{m/s})$
300	0.76	9455.4	453.1	1745.7	0.948	13.6	23.77	52.6	45.07

Table 3: Boundary layer properties at the station selected for the analysis ($x_a = 54.1\delta_i$) of the acoustic field for the present DNS. The local boundary layer thickness δ is approximately $\delta \approx 1.7\delta_i$.

2.3. *Validation of DNS data*

2.3.1. *Velocity statistics*

The velocity statistics (including the mean and RMS values) are reported in this section at a selected downstream location for statistical analysis ($x_a = 54.1\delta_i$), which are also used in the analysis of fluctuating pressure field in section 3. Table 3 lists the values of the mean boundary layer parameters at the selected location, including the momentum thickness θ, shape factor $H = \delta^*/\theta$ (where δ^* denotes the local displacement thickness). The outer and inner length scales (boundary layer thickness δ and viscous length scale z_τ, respectively) and the velocity scales u_τ and $u_\tau\sqrt{\rho_w/\rho_\infty}$ are also shown along with the representative Reynolds number parameters, $Re_\theta \equiv \rho_\infty U_\infty \theta/\mu_\infty$, $Re_\tau \equiv \rho_w u_\tau \delta/\mu_w$, and $Re_{\delta2} \equiv \rho_\infty U_\infty \theta/\mu_w$. Throughout this paper, the subscripts ∞ and w are used to denote quantities at the boundary layer edge and at the wall, respectively.

The van Driest transformed mean velocity profile based on the DNS is shown in figure 4. $\bar{U}_{VD}$ is defined as

$$\bar{U}_{VD} = \frac{1}{u_\tau}\int_0^U (\overline{T_w}/\overline{T})^{1/2}dU.$$

The mean velocity conforms well to the incompressible law-of-the-wall upon van Driest transformation and shows a (narrow) logarithmic region that is comparable in extent to Mach 4 simulations by Bernardini & Pirozzoli (2011) at similar Re_τ. In addition, the transformed mean-velocity profile compares well with the experimental results by Schlatter & Örlü (2010) for an incompressible boundary layer at $Re_\tau = 1145$ and by Bookey *et al.* (2005) at Mach 2.9, $Re_\tau = 501$.

Figures 5(a–f) plot turbulence intensities and density weighted turbulence intensities in streamwise, spanwise and wall-normal directions across the boundary layer. A significantly improved collapse of data is achieved by Morkovin's scaling, which takes into account the variation in mean flow properties. Morkovin's scaling brings the magnitudes of the extrema in the compressible cases closer to the incompressible results of Spalart (1988) and Schlatter & Örlü (2010), allowing the present DNS to compare well with existing data at similar conditions.

2.3.2. *Comparison with experiments*

The physical realism and accuracy of the computed flow fields have been further established by comparing with existing experimental results at similar flow conditions. Figure 6 shows the comparison of DNS results (Case M6Tw076) with the wind-tunnel measurement and the calculation using Harris Boundary-layer code (Harris & Blanchard 1982) for a Mach 5.8 turbulent boundary layer on the nozzle wall of BAM6QT under noisy-flow conditions ($Re = 9.69 \times 10^6/\text{m}$, $P_{t,\infty} = 965$ kPa, $T_{t,\infty} = 429$ K) (Casper 2011; Steen 2010). The DNS and experiments agree well with each other in terms of both boundary-layer profile and wall-pressure spectrum. In comparison, the Mach number profile based on the boundary layer code exhibits larger differences from the measurement
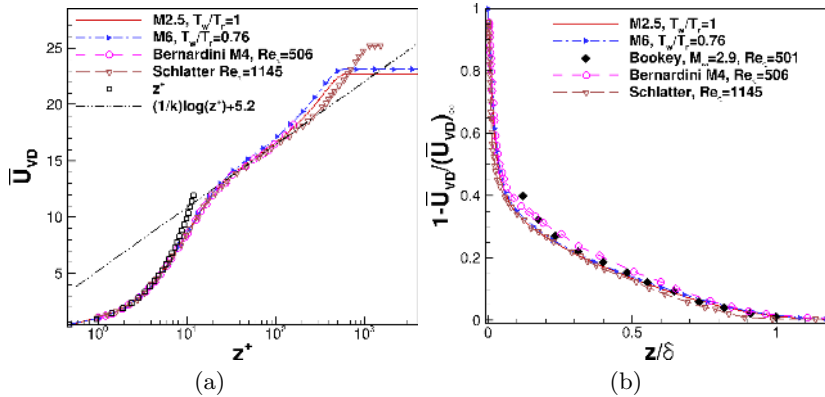
Figure 4: (a) van Driest transformed mean velocity profile (k=0.41, $C = 5.2$) and (b) van Driest transformed mean deficit velocity. Symbols denote the DNS by Bernardini & Pirozzoli (2011) at Mach 4, $Re_\tau = 506$ (circles), the experiment by Bookey *et al.* (2005) at Mach 2.9, $Re_\tau = 501$ (diamonds), and the experiment by Schlatter & Örlü (2010) for an incompressible boundary layer at $Re_\tau = 1145$ (gradients).

and the DNS in the outer part of the boundary layer. Moreover, figure 6c and figure 6d show that DNS extends the measured spectra to higher frequencies. The resolution of the high-frequency region as well as the acoustic radiation due to these high-frequency fluctuations are especially important for studying the receptivity process associated with second-mode waves in hypersonic wind tunnels.

Additional comparisons of DNS results with both experiments and other high-quality simulations are presented in the following sections.

3. Results

3.1. *Pressure Statistics*

Figures 7a shows that the RMS of pressure fluctuations normalized by the local wall shear for the present DNS and some of previous DNS results at lower Mach numbers with similar Reynolds numbers (Duan *et al.* 2014; Bernardini & Pirozzoli 2011). At the wall, the value of p'_{rms}/τ_w at Mach 5.86 is about 2.8, which is close to 3 based on the model by Bies (1966) and those given by the DNS of Guarini *et al.* (2000); Spalart (1988); Bernardini & Pirozzoli (2011) at lower Mach numbers. p'_{rms}/τ_w is insensitive to Mach number variation within most of the boundary layer and collapses with lower Mach-number data. Outside the boundary layer, however, p'_{rms}/τ_w approaches a constant value of about 0.9 for the Mach 5.86 case, which is significantly larger than the value of 0.4 for the Mach 2.5 turbulent boundary layer. The variation of freestream pressure fluctuations with Mach number is consistent with the trend predicted by the experimental data reported by Laufer (1964) (figure 7b). Whenever all four walls of the rectangular test section were radiating to the measurement location, Laufer obtained the contribution to the acoustic fluctuations from a single wall by assuming equal contributions from each wall. This assumption was validated by comparing the measured fluctuations with those in the case where only one wall had a turbulent boundary layer and the rest had laminar boundary layers. The increase in radiation intensity with freestream Mach number in figure 7b is consistent with the 'eddy Mach wave' hypothesis Phillips (1960), which states
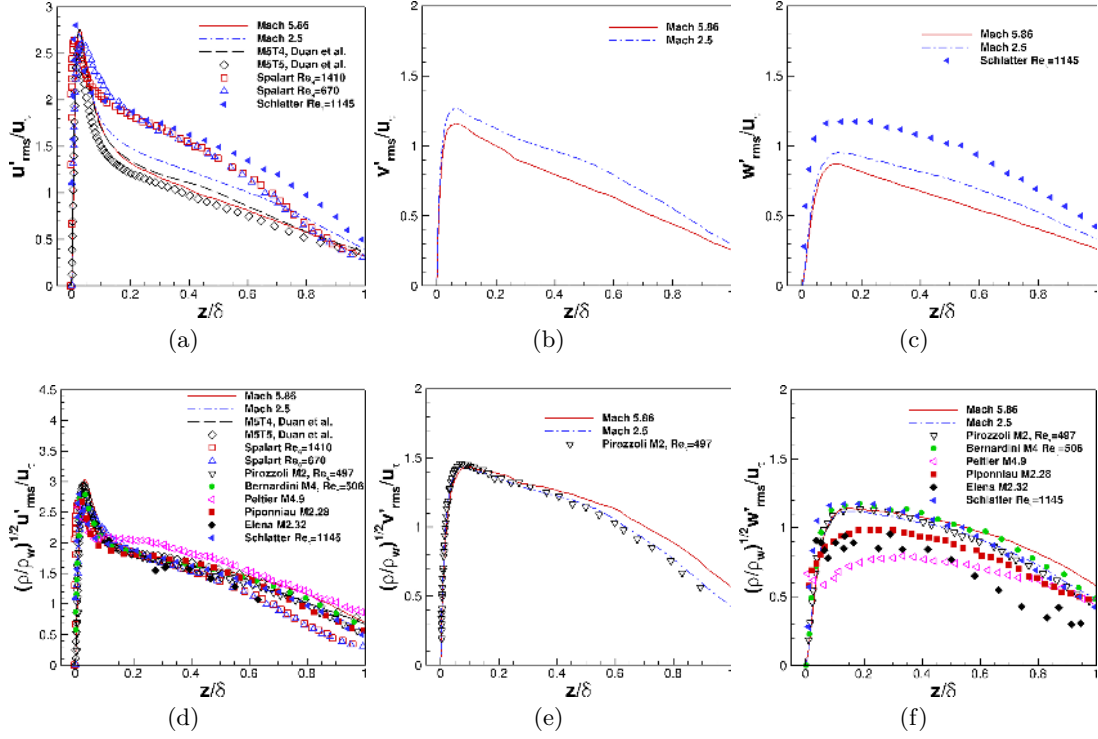
Figure 5: Turbulence intensities and density-weighted turbulence intensities of the (a,d) stream-wise, (b,e) spanwise and (c,f) wall-normal fluctuating velocity components. ————: Mach 5.86, $\mathbf{M_\infty = 5.86}$, $\mathbf{Re_\theta = 9455.4}$, $\mathbf{T_w/T_r = 0.76}$. —·—·—: Mach 2.5, $\mathbf{M_\infty = 2.5}$, $\mathbf{Re_\theta = 2834.8}$, $\mathbf{T_w/T_r = 1}$. – – –: M5T4 (Duan *et al.* 2010), $\mathbf{M_\infty = 5}$, $\mathbf{Re_\theta = 3819.3}$, $\mathbf{T_w/T_r = 0.68}$. ◇: M5T5 (Duan *et al.* 2010), $\mathbf{M_\infty = 5}$, $\mathbf{Re_\theta = 4840.5}$, $\mathbf{T_w/T_r = 1}$. □, (Spalart 1988), $\mathbf{M_\infty \approx 0}$, $\mathbf{Re_\theta = 1410}$. △, (Spalart 1988), $\mathbf{M_\infty \approx 0}$, $\mathbf{Re_\theta = 670}$. ▽, (Pirozzoli & Bernardini 2011), $\mathbf{M_\infty = 2, Re_\theta = 2377}$. ●, (Bernardini & Pirozzoli 2011), $\mathbf{M_\infty = 4, Re_\theta = 5824}$. ◁, (Peltier *et al.* 2012), $\mathbf{M_\infty = 4.9}$, $\mathbf{Re_\theta \approx 40 \times 10^3}$, $\mathbf{T_w/T_r = 0.9}$. ■, (Piponniau *et al.* 2009), $\mathbf{M_\infty = 2.28}$, $\mathbf{Re_\theta = 5100}$. ◆, (Eléna & Lacharme 1988), $\mathbf{M_\infty = 2.32}$, $\mathbf{Re_\theta = 4700}$. ◀, (Schlatter & Örlü 2010), $\mathbf{M_\infty \approx 0}$, $\mathbf{Re_\theta = 3626}$.

that the 'Mach wave type' radiation is produced by eddies that convect supersonically with respect to the free stream. At low supersonic freestream Mach numbers, sources that contribute primarily to the radiation field are slowly moving ones, the convection velocities of which are supersonic relative to the freestream (see figure 20). As the Mach number increases, additional faster moving turbulent eddies acquire supersonic relative speeds and start to take part in the radiation process, accounting for the larger acoustic amplitudes in the free stream.

3.2. *Frequency spectra*

The frequency spectrum of the pressure fluctuations is defined as

$$\Phi_p(\omega) = \frac{1}{2\pi} \int_{-\infty}^{\infty} \overline{p'(x,y,z,t)p'(x,y,z,t+\tau)} e^{-i\omega\tau} d\tau \qquad (3.1)$$
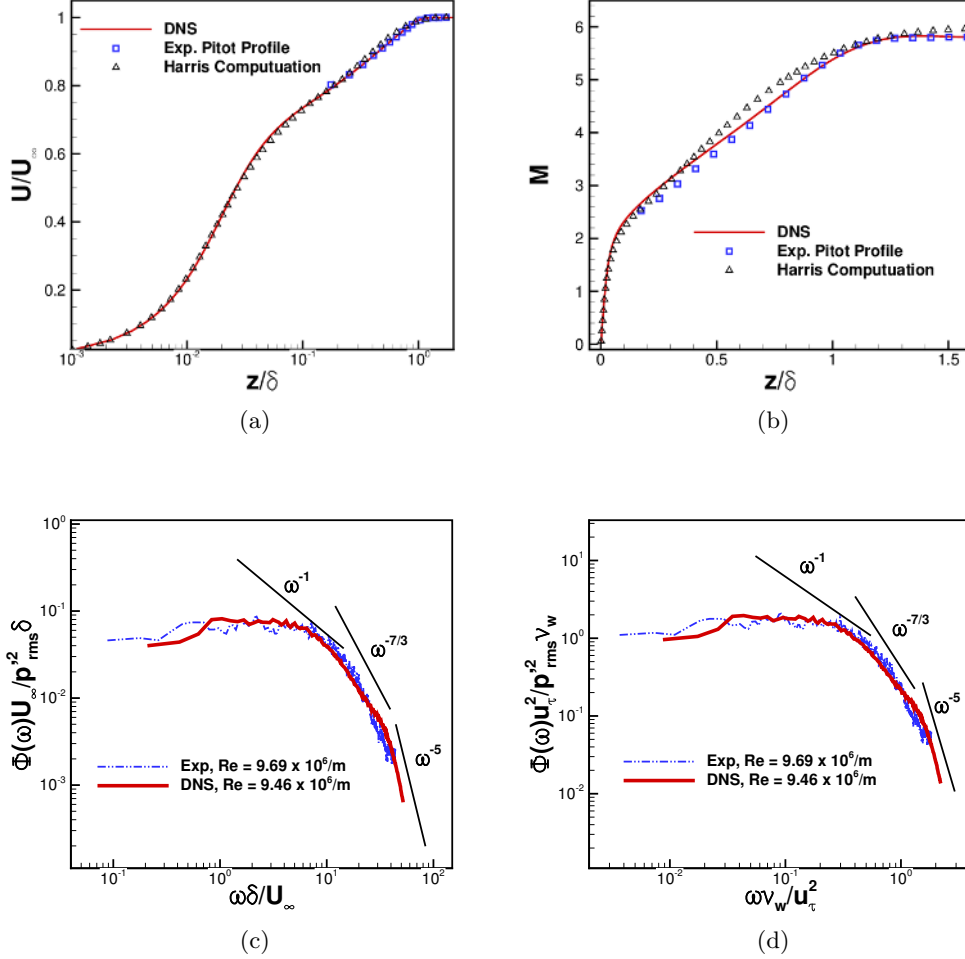
Figure 6: Comparison of DNS results with those of a Mach-5.8 turbulent boundary layer on the nozzle wall of the Boeing/AFOSR Mach-6 Quiet Tunnel under noisy-flow conditions ($Re = 9.69 \times 10^6$/m, $P_{t,\infty} = 965$ kPa, $T_{t,\infty} = 429$ K). The Pitot-probe measurement of the boudnary-layer profiles was conducted by Steen (2010); the calculation of the boundary-layer profiles using Harris boundary-layer Code (Harris & Blanchard 1982) and the measurement of the wall pressure spectrum were conducted by Casper (2011). The experimental curve of wall pressure spectrum is normalized with DNS-computed parameters and includes the Corcos correction for finite probe size (Beresh *et al.* 2011). (*a*) Mean velocity profile; (*b*) Mach number profile; (*c*) frequency spectrum in outer scale; (*d*) frequency spectrum in inner scale.

The pressure spectrum can be divided into several segments with different power law scalings. According to Bull (1996), the pressure spectrum can be broken into regions of low, mid, mid-to-high overlap, and high frequencies, with corresponding spectrum slopes of ω^2, ω^{-1}, $\omega^{-7/3}$, and ω^{-5}, respectively. The ω^2 dependence of pressure spectrum at lowest frequencies ($\omega\delta^*/U_\infty < 0.03$) are induced by the passive structures in the
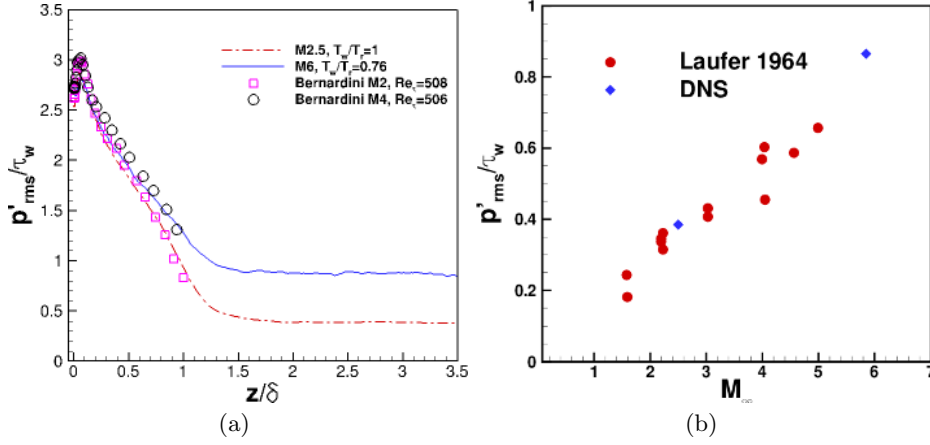
Figure 7: (a) Pressure fluctuation rms profile p'_{rms}/τ_w as a function of wall-normal distance. The symbols denote the DNS results of Bernardini & Pirozzoli (2011).(b) Comparison of p'_{rms}/τ_w in the free stream with the experiments by Laufer (1964), and the DNS results correspond to present case M6Tw076 and the Mach 2.5 results of Duan *et al.* (2014).

outer layer of the boundary layer. The ω^{-1} dependence of the pressure spectrum at mid frequencies is typically attributed to convected turbulence in the logarithmic region where the pressure-inducing eddies has a length scale proportional to the distance from the wall (Bradshaw 1967) . The $\omega^{-7/3}$ scaling of the pressure spectrum lies in the overlap region between mid and high frequencies and is attributed to eddies in the highest part of the buffer region ($20 < z^+ < 30$). Such a region is analogous to the inertial subrange in velocity spectra that is described by the Kolmogorov's $-5/3$ law. The typical frequency range for this region is $0.3 < \omega\nu/u_\tau^2 < 1$. The ω^{-5} dependence of the pressure spectrum at high frequencies is attributed to sources in the boundary layer below $z^+ = 20$ and this region is referred to as the sublayer dominance by Blake (1986).

Figure 8a shows the pressure spectrum as a function of the wall-normal distance for the present DNS. The pressure spectrum is normalized so that the area under each curve is equal to unity. For reference, straight lines with slopes of 2, -1, $-7/3$, and -5 are also included to gauge the rate of spectral roll-off across relatively low, mid, overlap, and high frequencies, respectively. The vertical lines in the plots ($\omega\nu_w/u_\tau^2 = 0.3$ and $\omega\nu_w/u_\tau^2 = 1.0$) demarcate the overlap regions between mid and high frequencies and show the estimated locations where a slope change in pressure spectrum is predicted according to the theory by Bull (1996).

The pressure spectrum shows a rather weak frequency dependence up to the lowest frequencies covered by the DNS ($\omega\delta^*/U_\infty \approx 0.08$). The absence of the more rapid and incompressible ω^2 scaling as $\omega \to 0$ at low frequencies in the wall-pressure spectrum is consistent with the measurements by Beresh *et al.* (2011); Casper (2011) and the DNS by Bernardini & Pirozzoli (2011) at supersonic Mach numbers. At all wall-normal locations, there is little evidence of the ω^{-1} region at mid-frequencies. Given that ω^{-1} dependence of the pressure spectrum is attributed to sources within the logarithmic region of the boundary layer, the absence of the ω^{-1} region is consistent with the relatively low Reynolds number ($Re_\tau \approx 500$) as well as the small logarithmic region of the current DNS. In the overlap region between the mid and high frequencies, the pressure spectrum

deviates from Kolmogorov's $-7/3$ scaling and shows a slope of $\omega^{-1.6}$ at the wall. As the location of interest moves away from the wall, the deviation from the Kolmogorov scaling becomes smaller. The deviation from the Kolmogorov scaling is expected given the non-zero shear rate within the boundary layer. As a result, local isotropy cannot be realized for the current Reynolds number (Tsuji *et al.* 2007). The reduced deviation from the Kolmogorov's $-7/3$ scaling away from the surface can be attributed to the progressive reduction in the local shear rate. The relation between the $\omega^{-7/3}$ scaling of the pressure spectrum and the shear rate has previously been explained by Bernardini *et al.* (2011), who observed the $\omega^{-7/3}$ behavior of wall-pressure spectrum in a supersonic turbulent boundary layer with adverse pressure gradient and showed that such a scaling is related to reduction of shear rate induced by adverse pressure gradient. At high frequencies, the spectrum exhibits a slightly more rapid decay than the ω^{-5} scaling predicted theoretically by Blake (1986), and the energy content becomes progressively lower as the location of interest moves away from the wall.

Figures 8b and 8c show a comparison of the pressure spectrum at the wall and in the free stream, respectively, for the present DNS at Mach 5.86 and that of a Mach 2.5 turbulent boundary layer (Duan *et al.* 2014). The higher Mach-number case exhibits significantly higher energy than the lower Mach number case at high frequencies. Similar dependence of pressure spectrum on Mach number was shown in the experiments by Laufer (1964). While an observable region of slope close to $-7/3$ is absent in the freestream pressure spectrum of the Mach 5.86 DNS, the freestream spectrum for the Mach 2.5 case has an observable region of slope close to $-7/3$, indicating a possible influence of Mach number on the overlap region of the pressure spectrum. A similar Mach-number dependence of the freestream pressure spectrum has been observed by Masutti *et al.* (2012).

To illustrate the distribution of energy among various frequencies, figure 9a shows the pre-multiplied pressure spectra at selected heights above the surface. It is shown that the pressure spectra in the inner layer have a dominant hump centered on $\omega\delta/U_\infty \approx 8$ (or $f\delta/U_\infty \approx 1$), which is the characteristic frequency of the energetic vortical structures within the boundary layer. As one moves away from the wall into the outer layer, the peak gradually shifts to lower frequencies as spatial intermittency becomes more important. In the free stream, where the pressure signal is predominantly acoustic, the peak of the spectrum is centered at a frequency of $\omega\delta/U_\infty \approx 3$ (i.e. $f \approx 10.8$ kHz), indicating that characteristic frequency of the acoustic fluctuations is significantly lower than that of the vorticity mode. Similar variation in pre-multiplied pressure spectrum with wall-normal distance is observed for the Mach 2.5 case. Figure 9b further compares the pre-multiplied spectra for the two Mach number cases at the wall and in the free stream. While the wall spectrum is centered on nearly the same frequency $\omega\delta/U_\infty \approx 8$ at both Mach numbers, the freestream spectrum for the Mach 5.86 case peaks at significantly higher frequency than the Mach 2.5 case. The reduced gap in the dominant frequency between pressure signals at the wall and in the free stream can be explained by the 'eddy Mach wave radiation' concept (Phillips 1960; Ffowcs-Williams & Maidanik 1965). As the Mach number increases, additional faster moving turbulent eddies acquire supersonic relative speeds and start in the radiation process. The increased fraction of the inner layer that can radiate to the free stream contributes to a reduced gap between the peak frequency of fluctuations near the surface and in the free stream.
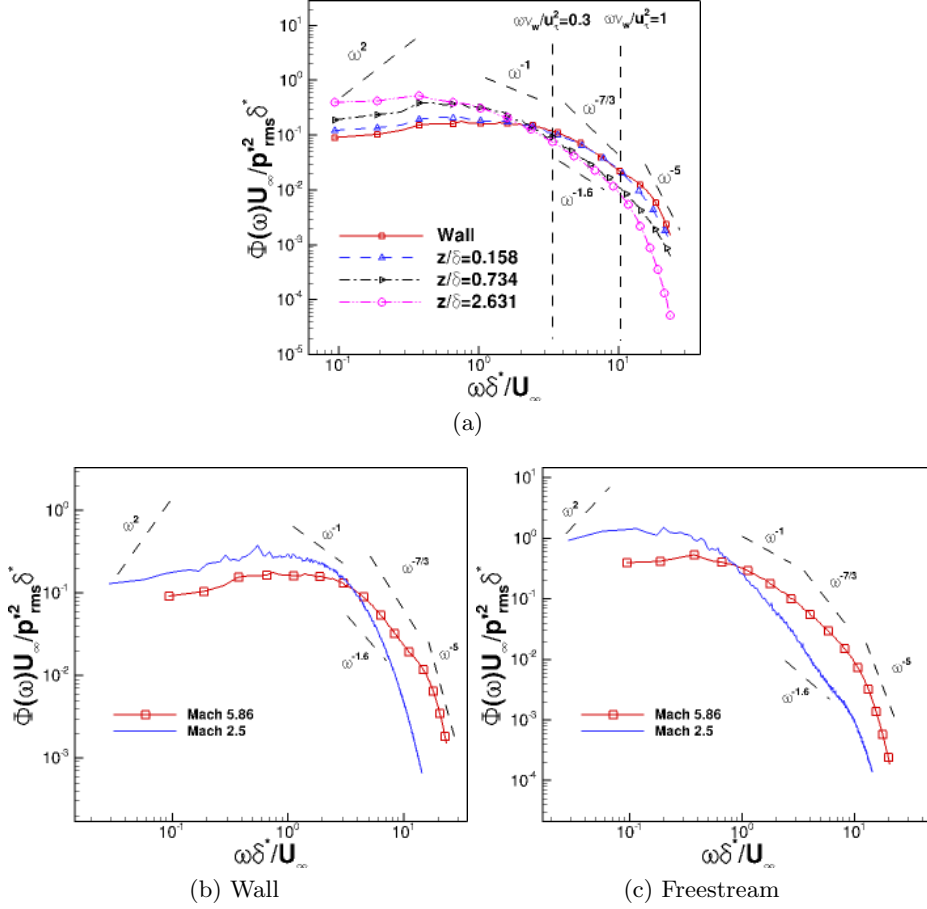
(a)

(b) Wall   (c) Freestream

Figure 8: (a) Normalized frequency spectrum of computed pressure signal at selected heights for the Mach 5.86; (b), (c) Comparison of pressure spectrum at the wall and in the free stream between the Mach 5.86 DNS and the Mach 2.5 DNS Duan *et al.* (2014). The freestream are taken at $z/\delta = 2.63$ for the Mach 5.86 DNS and $z/\delta = 2.8$ for the Mach 2.5.

3.3. *Two-point correlations*

3.3.1. *Two-point correlations in streamwise-spanwise planes*

The two-point correlation coefficient of the pressure field in a streamwise-spanwise plane is defined as

$$C_{pp}(\Delta x, \Delta y, z) = \frac{\overline{p'(x,y,z,t)p'(x+\Delta x, y+\Delta y, z, t)}}{\left(\overline{p'^2(x,y,z,t)}\right)^{1/2}\left(\overline{p'^2(x+\Delta x, y+\Delta y, z, t)}\right)^{1/2}} \qquad (3.2)$$

where Δx and Δy are spatial separations in the streamwise and spanwise directions, respectively.

Figure 10 displays the contours of streamwise-spanwise correlation $C_{pp}(\Delta x, \Delta y, z)$ of the pressure fluctuations across a range of wall-normal heights for the present DNS and the Mach 2.5 case of Duan *et al.* (2014). The contours of C_{pp} are approximately circular for small spatial separation but become elongated in the spanwise direction for large sep-
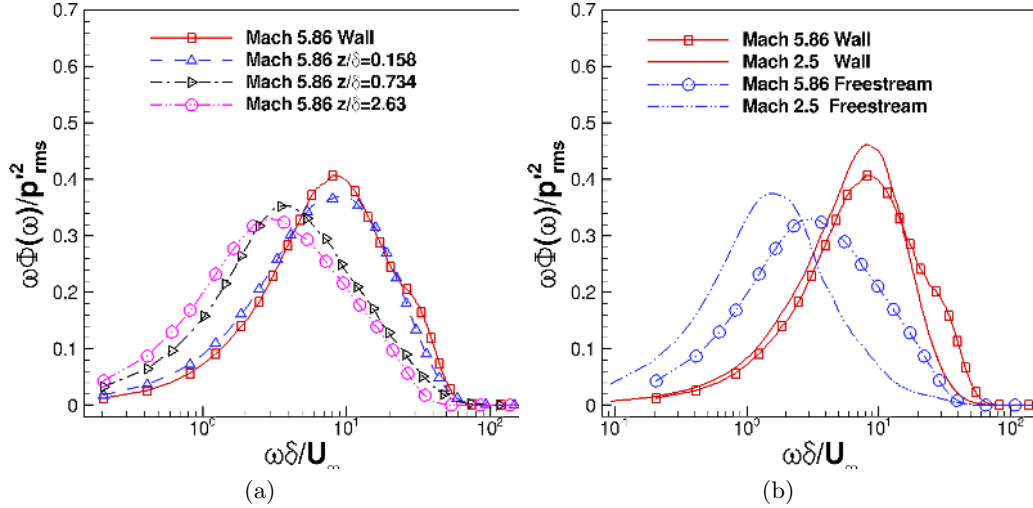
Figure 9: Pre-multiplied power spectrum of pressure signals. (a) at selected heights for the Mach 5.86 DNS; (b) comparison between Mach 5.86 and Mach 2.5 Duan *et al.* (2014). The pressure spectrum is normalized so that the area under each curve is equal to unity. The freestream are taken at $z/\delta = 2.63$ for the Mach 5.86 DNS and $z/\delta = 2.8$ for the Mach 2.5.

aration distances, indicating that the small-scale pressure-carrying eddies or wavepackets are nearly isotropic while the large-scale eddies become more coherent in the spanwise direction. The extent of the pressure contours increases in both in-plane directions as the wall-normal height increases. The two-point correlations of the pressure fluctuations in the free stream show similar patterns to those within the boundary layer, except for a variation in spatial length scales. Within the boundary layer, the pressure contours exhibit minor Mach number dependence when nondimensionalized by the boundary layer thickness. In the free stream, however, the large-scale pressure wavepackets for the Mach 5.86 case become less elongated in the spanwise direction compared with the lower Mach number case.

Figures 11a and 11b show the variation of streamwise and spanwise length scales of the pressure field $((L_x)_p$ and $(L_y)_p)$, respectively, as a function of wall-normal distance.

The streamwise and spanwise length scales of the pressure field display an approximate increase with wall-normal coordinate within most of the boundary layer, reaching a peak just outside the boundary-layer edge. For about $z/\delta > 2$, both scales again relax to approximately constant values that are nearly twenty-five percent lower than the respective peaks. Such a dependence of length scales on the wall-normal coordinate is consistent with wall-normal variation of the extent of pressure correlation contours shown in figure 10. The nearly linear increase of pressure length scales with wall-normal location in the outer region of the boundary layer is consistent with the conceptual model of very large-scale motion (VLSM) proposed by Kim & Adrian (1999). Similar wall-normal variation of large-scale coherence has been revealed by PIV experiments of turbulent boundary layers at low and supersonic speeds (Tomkins & Adrian 2003; Ganapathisubramani *et al.* 2005, 2006) based on two-point correlations of streamwise velocity fluctuations.

(a) wall

(b) $z/\delta = 0.158$

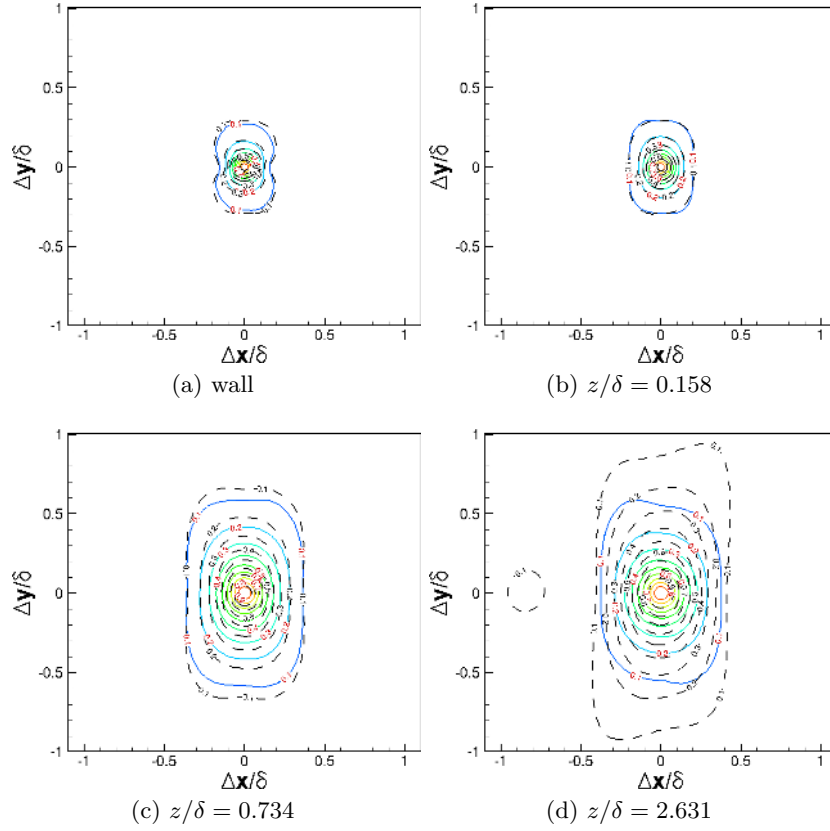(c) $z/\delta = 0.734$

(d) $z/\delta = 2.631$

Figure 10: Contours of constant streamwise-spanwise correlation coefficient of the pressure signal $C_{pp}(\Delta x, \Delta y)$ at selected heights for Mach 5.86 (Colored solid line) and Mach 2.5 (Black dashed line). Contour levels vary from 0.1 to 0.9 with increments of 0.1.
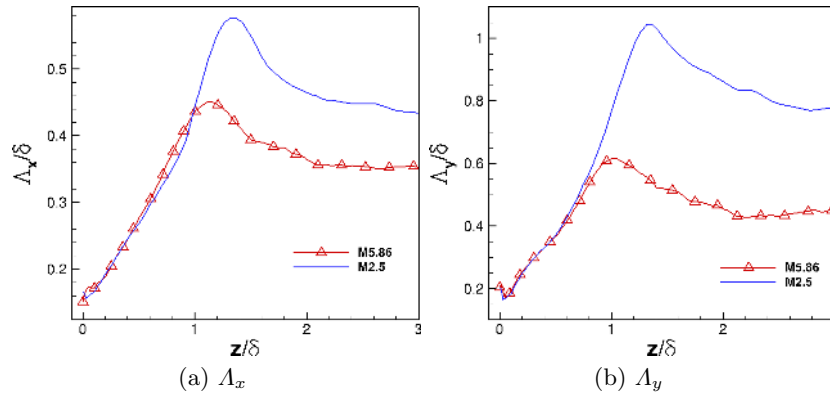

(a) Λ_x

(b) Λ_y

Figure 11: (a) Streamwise Λ_x and (b) spanwise Λ_y integral length scales as a function of the wall-normal location. $\Lambda_x \equiv \int C_{pp}(\Delta x, 0, 0)d(\Delta x)$ and $\Lambda_y \equiv \int C_{pp}(0, \Delta y, 0)d(\Delta y)$, with the limits of the integral chosen as the streamwise and spanwise separations between the two crossings of $C_{pp} = 0.1$.

3.3.2. *Two-point correlations in streamwise wall-normal planes*

The two-point correlation coefficient of the pressure field in a streamwise wall-normal plane is defined as

$$C_{pp}(\Delta x, z, z_{ref}) = \frac{\overline{p'(x,y,z_{ref},t)p'(x+\Delta x,y,z,t)}}{\left(\overline{p'^2(x,y,z_{ref},t)}\right)^{1/2} \left(\overline{p'^2(x+\Delta x,y,z,t)}\right)^{1/2}} \quad (3.3)$$

where Δx is spatial separations in the streamwise direction and z_{ref} is the reference wall-normal location at which the correlation is computed.

Contours of constant $C_{pp}(\Delta x, z, z_{ref})$ for the present Mach 5.86 DNS at multiple reference heights z_{ref} are shown in figure 12. The same contours for the Mach 2.5 DNS (Duan *et al.* 2014) are also included to highlight the differences from the lower Mach number case. For each reference height z_{ref}, the maximum correlation of pressure fluctuations is approximately aligned along a line, indicating the presence of downward-leaning structures. At the wall,the structure of pressure fluctuations is inclined about $\theta_{xz} \approx 80°$ to the wall. The inclination angle decreases gradually in the inner and outer regions of the boundary layer. In the free stream, the inclination angle of the pressure structure plateaus to $\theta_{xz} \approx 21°$, and the freestream wave-front inclination θ_{xz} closely matches the wave-front orientation of the instantaneous acoustic radiation visualized by numerical Schlieren as shown in figure 19a. The variation in θ_{xz} with wall-normal distance indicates that pressure disturbances generated within the boundary layer will undergo significant refraction before they are radiated to the free stream. The freestream pressure wave-front inclination θ_{xz} closely matches the wave-front orientation of the instantaneous acoustic radiation visualized by numerical Schlieren as shown in figure 19a.

The pressure-structure angle exhibits minor Mach number dependence within the boundary layer. In the free stream, however, the pressure wave front is significantly shallower for the higher Mach number case. The shallower wave front of the freestream radiation for the higher Mach number case is consistent with the decrease in the zone of influence of a flow disturbance as Mach number increases.

3.3.3. *Space-time correlation*

The space-time of the pressure field is defined as

$$C_{pp}(\Delta x, \Delta t) = \frac{\overline{p'(x,y,z,t)p'(x+\Delta x,y,z,t+\Delta t)}}{\left(\overline{p'^2(x,y,z,t)}\right)^{1/2} \left(\overline{p'^2(x+\Delta x,y,z,t+\Delta t)}\right)^{1/2}} \quad (3.4)$$

where Δx and Δt are spatial separation in the streamwise direction and the time delay, respectively.

The space-time correlation contours of $C_{pp}(\Delta x, \Delta t)$ are plotted at multiple wall-normal locations as shown in figure 13. For comparison, the same contours for the Mach 2.5 DNS (Duan *et al.* 2014) are also included. At all wall-normal locations, the pressure contours are skewed with the maximum correlation aligned along the first or third quadrant in the $(\Delta x, \Delta t)$-plane. The concentration of contours of $C_{pp}(\Delta x, \Delta t)$ into a narrow band indicates strong downstream propagation of pressure fluctuations. In addition, there is a change in the overall slope of $d\Delta x/d\Delta t$ at different wall-normal locations, indicating a variation of bulk propagation speed of pressure fluctuations as a function of wall-normal distance. The overall larger inclination of the space-time correlation contours in the free stream for the Mach 5.86 case indicates that the freestream pressure structures propagate with a larger speed relative to the Mach 2.5 case. A further discussion of the propagation

(a) $z_{ref}/\delta = 0$

(b) $z_{ref}/\delta = 0.158$

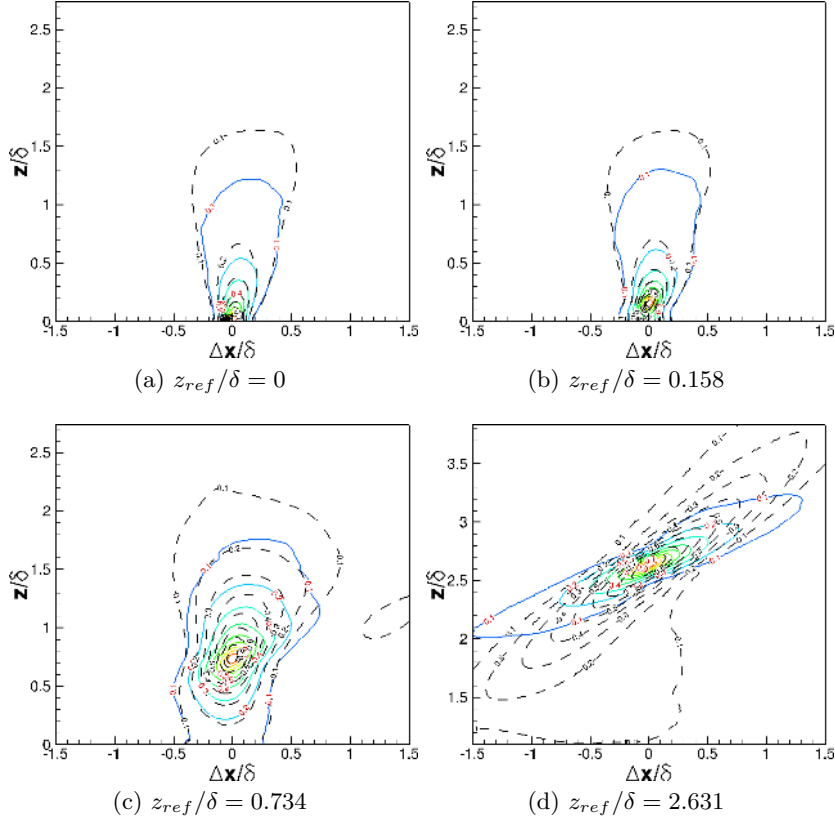(c) $z_{ref}/\delta = 0.734$

(d) $z_{ref}/\delta = 2.631$

Figure 12: Streamwise wall-normal correlation coefficient of the pressure signal $C_{pp}(\Delta x, z, z_{ref})$ at selected heights for Mach 5.86 (Colored solid line) and Mach 2.5 (Black dashed line). Contour levels vary from 0.1 to 0.9 with increments of 0.1.

speed of pressure fluctuations, including its dependence on different definitions, will be given in section 3.4.

Figures 14a and 14b plot the maximum space-time correlation of pressure fluctuations, $(C_{pp})_{max}$, as a function of time delay Δt and streamwise separation Δx, respectively, at multiple wall-normal locations. The scales of temporal and spatial decays in $(C_{pp})_{max}$ are measures of the life time and Lagrangian decorrelation length of the coherent pressure structures or wavepackets. Within the boundary layer, the temporal and spatial Lagrangian scales of the pressure structures increase with wall-normal distance and are at least five times larger than the large-eddy turnover time and the boundary layer thickness, respectively. In the free stream, the acoustic pressure fluctuations show similar temporal and spatial decay rates as those near the wall ($z^+ \approx 20$). Given that acoustic sources are concentrated in the near-wall region according to the concept of 'eddy Mach-wave radiation' (section 4.3), the apparent match in the Lagrangian time and spatial scales between the freestream pressure structures and the structures near the wall indicates that the freestream acoustic radiation mainly originates from the near-wall region, a finding that is consistent with the concept of 'eddy Mach waves'.
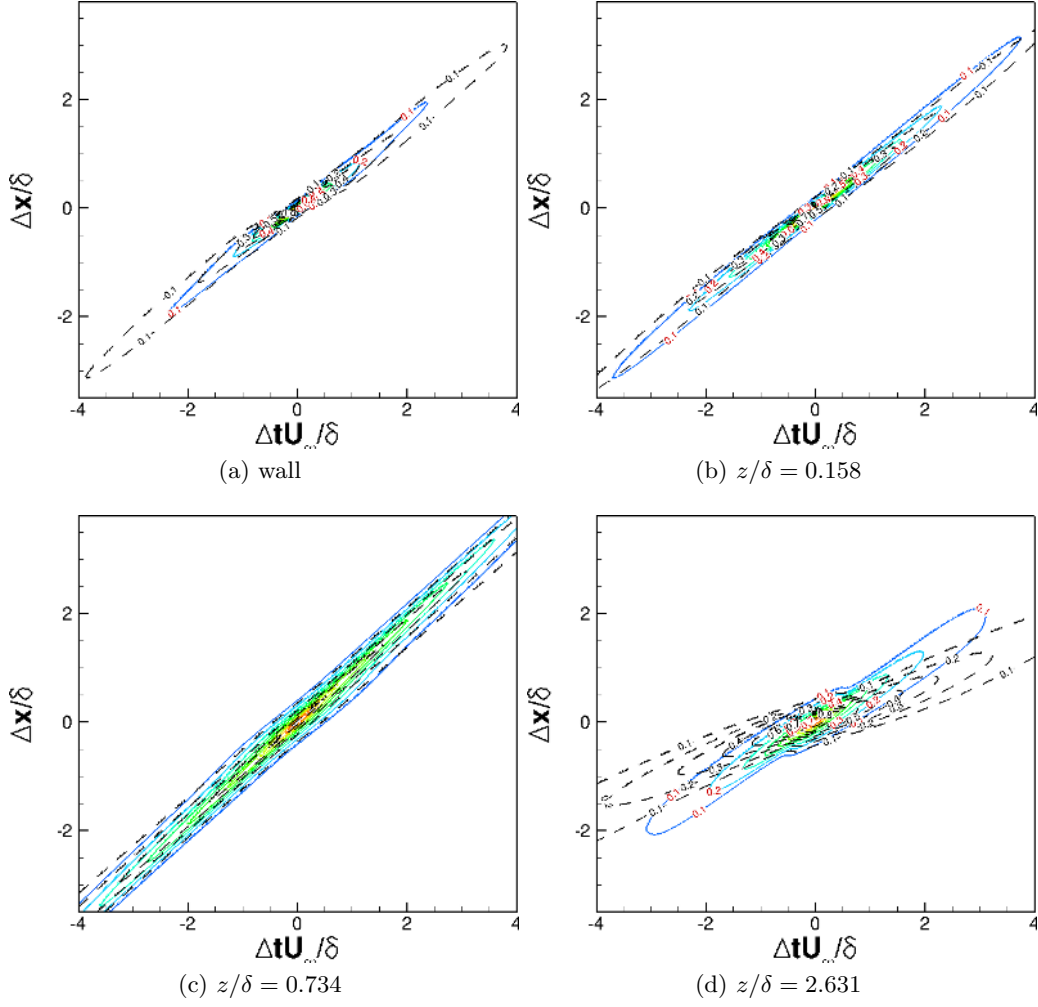
Figure 13: Contours of constant space-time correlation coefficient of pressure fluctuations $C_{pp}(\Delta x, \Delta t)$ at selected heights for Mach 5.86 (Colored solid line) and Mach 2.5 (Black dashed line). Contour levels vary from 0.1 to 0.9 with increments of 0.1.

3.4. Propagation speed

The space-time correlation data based on the DNS was used to estimate the speed of propagation of pressure fluctuations. First, for a given time delay Δt, the propagation speed U_c is defined as the ratio $\Delta x/\Delta t$ at the value of Δx where

$$\left.\frac{\partial C(r_x, 0, \Delta t)}{\partial r_x}\right|_{r_x=\Delta x} = 0 \qquad (3.5)$$

Similar procedure has been used by multiple researchers (Kim 1989; Choi & Moin 1990; Bernardini & Pirozzoli 2011) to define the convection speed of wall-pressure fluctuations. Figure 15a plots the propagation speed as a function of time delay Δt at several selected heights across the boundary layer for the present DNS. As expected, the propagation speed shows a Δt dependence, and there is an increase in U_c at large time separations
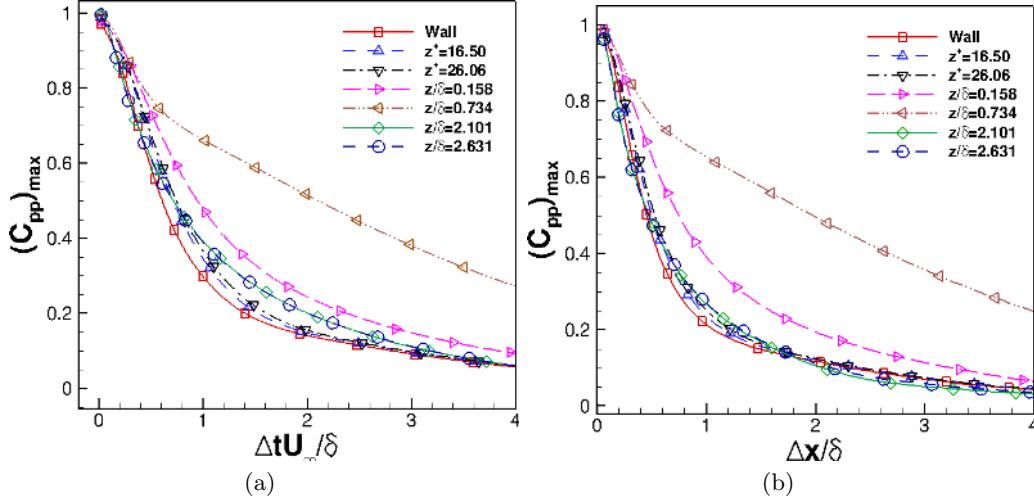
Figure 14: Decay of the maximum spatial-time correlation coefficient of pressure fluctuations, $(C_{pp})_{max}$, as a function of (a) time delay Δt and (b) streamwise separation Δx.

in the inner and outer layers of the boundary layer ($z/\delta < 1$). Given that only large eddies retain their coherence at large time separations, such an increase in U_c at large Δt may suggest that large pressure-carrying eddies/wavepackets propagate with higher speeds than small ones. The propagation speed at the wall is $U_c \approx 0.8U_\infty$ for the large-scale disturbances (associated with large time delay) and $U_c \approx 0.72U_\infty$ for the small-scale disturbances (associated with small time delay). The magnitude of the propagation speed near the surface as well as its scale dependence is in close agreement with both measured and computed values for low-speed and supersonic turbulent boundary-layer flows (Willmarth 1975; Choi & Moin 1990; Tsuji *et al.* 2007; Bernardini & Pirozzoli 2011). The propagation velocity becomes less scale dependent in the log layer ($z/\delta = 0.16$) and the outer layer ($z/\delta = 0.73$) and the overall range is very close to the local mean velocity. Outside the boundary layer, the propagation speed is again insensitive to Δt and the pressure wavepackets propagate at a significantly smaller speed of $U_c \approx 0.63U_\infty$. Similar findings were reported by Duan *et al.* (2014) for a Mach 2.5 turbulent boundary layer. The significantly smaller propagation speed of the freestream pressure wavepackets indicates that the acoustic sources that radiate noise into the freestream convect with a speed much smaller than the freestream velocity.

As suggest by Laufer (1964), the propagation speed $U_c \equiv \Delta x/\Delta t$ can also be defined for a given Δx and at the value of Δt where

$$\left.\frac{\partial C(\Delta x, 0, r_t)}{\partial r_t}\right|_{r_t=\Delta t} = 0 \tag{3.6}$$

This definition is consistent with Laufer's experiments (Laufer 1964) in which two probes with fixed streamwise separation are used to determine the propagation speed. Figure 15b shows a plot of the propagation speed U_c as a function of streamwise separation Δx at selected wall-normal locations. Similar to figure 15a, the propagation speed in the inner layer increases at large streamwise separations and such an increase becomes less significant as the location of interest moves to the outer layer. In the free stream, U_c/U_∞ is
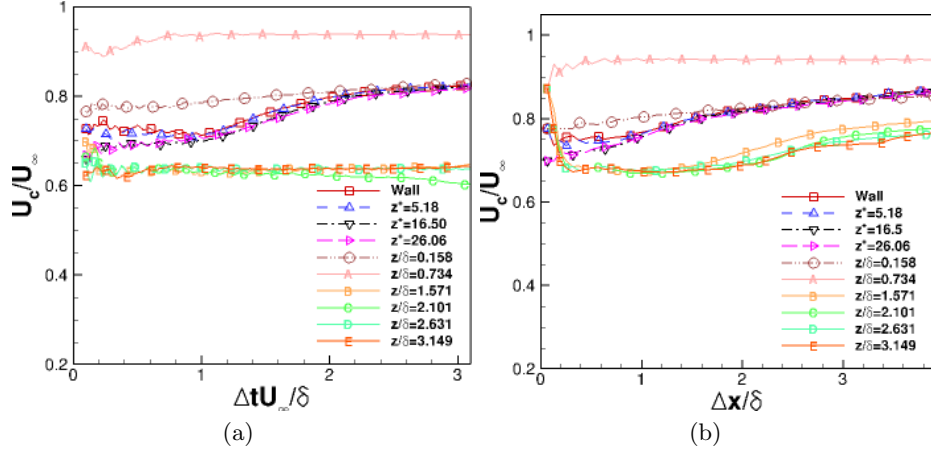
Figure 15: Propagation speed of pressure fluctuations as a function of (a) time delay Δt and (b) streamwise separation Δx for the DNS of Mach 5.86 turbulent boundary layer.

approximately 0.68 for $\Delta x/\delta \approx 0.23$ (corresponding to the probe separation $\Delta x_{Laufer} = 0.71$ centimeters in Laufer's experiment by assuming $\delta_{Laufer} = 3.15$ centimeters).

A third way to quantify the overall propagation speed of pressure-carrying eddies or wavepackets is to find the value of U_b which minimizes the difference between the real time evolution of $p(x, t)$ and a frozen wave $p(x - U_b t)$. Following this definition, the following expression can be obtained

$$U_b \equiv -\frac{\overline{(\partial p/\partial t)(\partial p/\partial x)}}{\overline{(\partial p/\partial x)^2}} \tag{3.7}$$

The same definition of bulk propagation speed was introduced by Del Alamo & Jimenez (2009) for the streamwise velocity fluctuations. Similar to the streamwise velocity (Del Alamo & Jimenez 2009), a figure of merit for the frozen-wave approximation can be introduced for the pressure fluctuations as

$$\gamma_p \equiv \frac{\left|\overline{(\partial p/\partial x)(\partial p/\partial t)}\right|}{\left[\overline{(\partial p/\partial t)^2}\ \overline{(\partial p/\partial x)^2}\right]^{1/2}} \tag{3.8}$$

γ_p equals to unity for a perfect frozen wave, and zero for fast decaying or deforming waves as they convect downstream.

Figure 16 plots the bulk propagation speed of the pressure fluctuation as a function of wall-normal distance. The bulk propagation speed of the pressure fluctuation is significantly larger than the local mean velocity in the viscous sublayer and the buffer layer. The bulk propagation speed of the pressure fluctuation becomes approximately equal to the local mean velocity in the upper buffer layer and remains so over a significant portion of boundary layer (up to $z/\delta \approx 0.65$). Such a variation of U_b within the boundary layer is consistent with the findings for incompressible and lower-Mach-number supersonic flows (Kim & Hussain 1993; Duan *et al.* 2014). In the free stream, the propagation speed departs from the Taylor's hypothesis and is significantly lower than the local mean velocity. Figure 17 shows the wall-normal distribution of the correlation coefficient γ_p that provides a figure of merit for the frozen-wave approximation. The pressure wave is nearly frozen with $\gamma \approx 1$ within the boundary layer and becomes less so outside the boundary
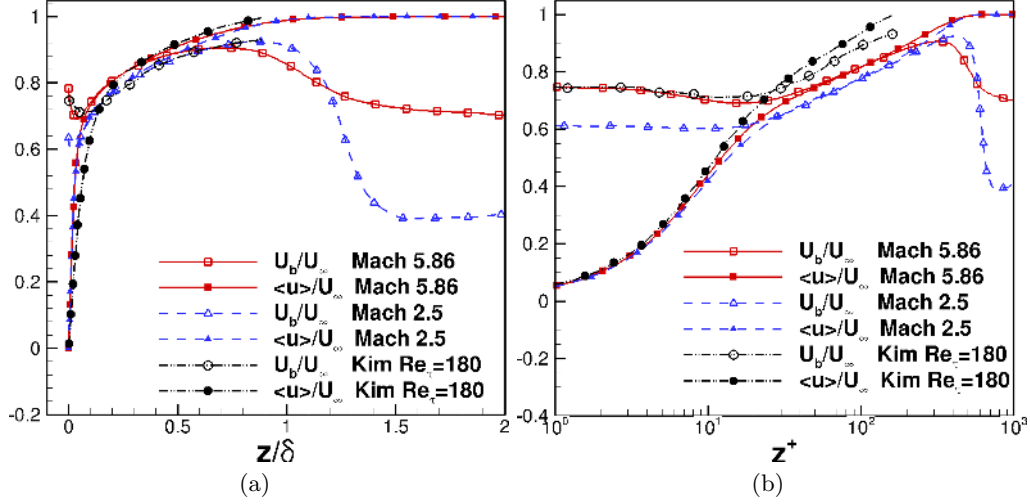
Figure 16: Wall-normal distribution of bulk propagation speed of pressure fluctuations in (a) outer and (b) inner units. U_b is defined based on 'frozen-wave' approximation as equation 3.7 (Del Alamo & Jimenez 2009) for the Mach 5.86 and Mach 2.5 DNS, and is calculated using equation 3.5 with $\Delta t^+ = 18$ for the incompressible DNS by Kim & Hussain (1993).

layer at both Mach numbers. As the Mach number increases, propagation effect becomes significantly more dominant over evolution effect for the freestream pressure wave.

Figure 18 compares the bulk propagation speed at the wall and in the free stream with some existing experiments and simulations. In the figure, U_{b1} is defined based on the space-time correlation coefficient with equation 3.5 for the time delay Δt or frequency ($\omega = 2\pi/\Delta t$) where the pre-multiplied frequency spectrum (figure 9a) attains its maximum. In analogy, U_{b2} is derived based on equation 3.6 for the streamwise separation Δx or wavenumber ($k_1 = 2\pi/\Delta x$) where the pre-multiplied one-dimensional wavenumber spectrum attains its maximum. U_{b3} is computed using equation 3.7 by assuming 'frozen wave/eddy'. The values of bulk propagation speed U_b varies depending on specific definitions. Similar findings were reported for the convection speed of the wall pressure (Choi & Moin 1990). The value of U_b at the wall gradually increases with the freestream Mach number and is slightly higher than those widely quoted for low-speed flows (Willmarth 1975; Choi & Moin 1990; Tsuji *et al.* 2007). The gradual increase in propagation speeds with Mach number is consistent with the values reported by Bernardini & Pirozzoli (2011) for turbulent boundary layers at Mach 2, 3, and 4 (figure 18a). In the free stream, the bulk propagation speed is approximately equal to $0.7U_\infty$. Such a freestream propagation speed falls within the region where $M_r > 1$, with $M_r \equiv (U_\infty - U_b)/a_\infty$, consistent with the concept of 'eddy Mach wave' radiation (Phillips 1960; Ffowcs-Williams & Maidanik 1965). Figure 18b further shows that the DNS-computed propagation speed compares well with existing experiments and simulations (Laufer 1964; Duan *et al.* 2014).
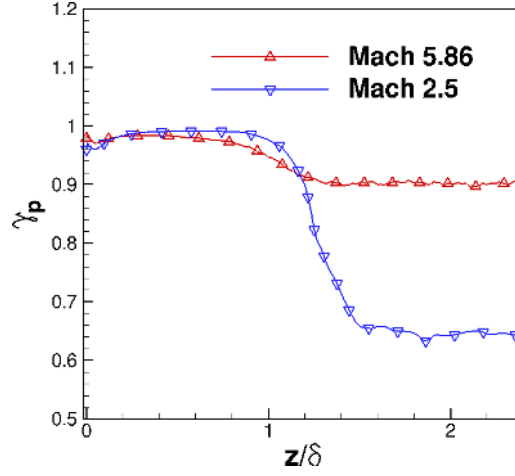
Figure 17: The distribution of correlation coefficient $\gamma_p = \frac{|\overline{(\partial p/\partial x)(\partial p/\partial t)}|}{\left[\overline{(\partial p/\partial t)^2} \ \overline{(\partial p/\partial x)^2}\right]^{1/2}}$ that provides a figure of merit for the frozen-wave approximation.
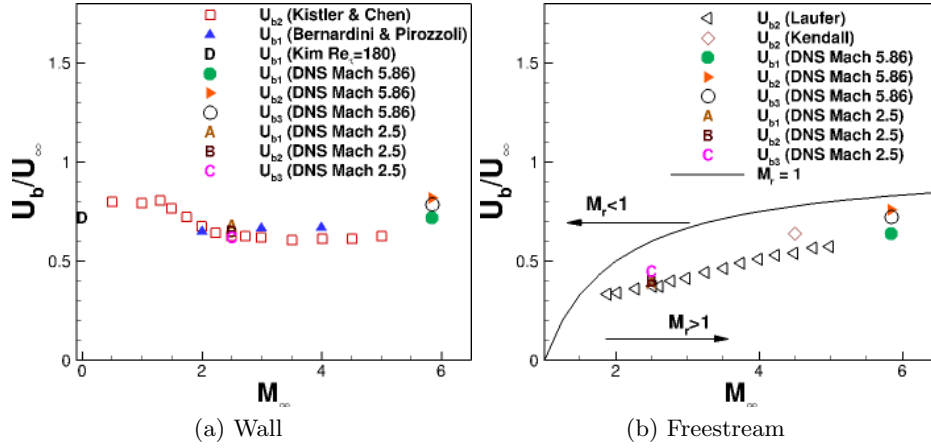

(a) Wall

(b) Freestream

Figure 18: Bulk convection speed of pressure fluctuations as a function of freestream Mach number: (a) at the wall; (b) in the freestream. Symbols: *squares*: Kistler & Chen (1963); *deltas*: Bernardini & Pirozzoli (2011); *left triangles*: Laufer (1964); *diamonds*: Kendall (1970); *D*: Kim (1989); *filled circles*: DNS Mach 5.86; *right triangles*: DNS Mach 5.86; *circles*: DNS Mach 5.86; *A*: DNS Mach 2.5 (Duan *et al.* 2014); *B*: DNS Mach 2.5; *C*: DNS Mach 2.5; *Lines*: $M_r = 1$. $U_{b1} : \frac{\partial C(r_x,0,\Delta t)}{\partial r_x}|_{r_x=\Delta x} = 0$, $U_{b1} : \frac{\partial C(\Delta x,0,r_t)}{\partial r_t}|_{r_t=\Delta t} = 0$. $U_{b3} : -\frac{\overline{(\partial p/\partial t)(\partial p/\partial x)}}{\overline{(\partial p/\partial x)^2}}$.

4. Freestream acoustic radiation

4.1. *Characteristics of Freestream fluctuations*

In this section, the nature of freestream acoustic fluctuations is analyzed using the present DNS data at Mach 5.86 and compared with previous results at Mach 2.5 Duan *et al.* (2014).

Table 4 lists the freestream values of several fluctuating flow variables for the present

	Mach 5.86	Mach 2.5
$u'_{rms}/\overline{u}$	1.3633×10^{-3}	8.3217×10^{-4}
$v'_{rms}/\overline{u}$	1.0514×10^{-3}	4.9146×10^{-4}
$w'_{rms}/\overline{u}$	2.0526×10^{-3}	9.1447×10^{-4}
$p'_{rms}/\overline{p}$	2.0498×10^{-2}	3.9143×10^{-3}
$\rho'_{rms}/\overline{\rho}$	1.4621×10^{-2}	2.7967×10^{-3}
$T'_{rms}/\overline{T}$	5.8908×10^{-3}	1.1180×10^{-3}
$(\rho u)'_{rms}/\overline{\rho u}$	1.3754×10^{-2}	2.2742×10^{-3}
$T'_{t,rms}/\overline{T}_t$	1.9813×10^{-3}	6.5962×10^{-4}
$p'_{t,rms}/\overline{p}_t$	6.6867×10^{-3}	2.3330×10^{-3}
$\overline{(\partial u_i/\partial x_i)'^2}/\overline{\Omega'_i \Omega'_i}$	31580	6099
s'_{rms}/R	2.1149×10^{-3}	1.1765×10^{-4}
$\overline{u'p'}/u'_{rms}p'_{rms}$	-0.6528	-0.7197
$\overline{v'p'}/v'_{rms}p'_{rms}$	-0.00639	-0.0059
$\overline{w'p'}/w'_{rms}p'_{rms}$	0.9250	0.7765
$\overline{\rho'p'}/\rho'_{rms}p'_{rms}$	1	1
$\overline{T'p'}/T'_{rms}p'_{rms}$	1	1

Table 4: The disturbance field at $z/\delta = 2.63$ for Case Mach 5.86 and $z/\delta = 2.8$ for Case Mach 2.5.

DNS at Mach 5.86 and the Mach 2.5 DNS (Duan *et al.* 2014). Similar to the Mach 2.5 case, the freestream thermodynamic fluctuations for the present Mach 5.86 case satisfy isentropic relations, indicating the acoustic nature of freestream fluctuations. Moreover, the level of dilatational fluctuations $\overline{(\partial u_i/\partial x_i)'^2}$, which is representative of the acoustic mode, is compared with the magnitude of vortical fluctuations $\overline{\Omega'_i \Omega'_i}$, which is representative of vorticity mode. The large values of $\overline{(\partial u_i/\partial x_i)'^2}/\overline{\Omega'_i \Omega'_i}$ as well as the small values of entropy fluctuations s'_{rms}/R relative to $p'_{rms}/\overline{p}$ imply that the acoustic mode is dominant over the vorticity and entropy modes in the free stream in terms of modal compositions (Kovasznay 1953). The dominance of the acoustic mode over the other two modes confirms that a purely acoustic field in the free stream is successfully isolated by the present DNS. Thus, the present simulation provides a unique opportunity for studying the similarities and differences in the characteristics of the primarily vortical fluctuations within the boundary layer and acoustic fluctuations in the free stream.

The normalized velocity fluctuations at Mach 5.86 are significantly larger than those at Mach 2.5. Yet, the rms fluctuations in either velocity component are less than approximately 0.25%. The fluctuations in thermodynamic variables are stronger than the velocity fluctuations and also increases from Mach 2.5 to Mach 5.86. At Mach 5.86, the rms pressure fluctuations are approximately 2% of the mean pressure value, compared with $\overline{p'_{rms}}/\bar{p} \approx 0.4\%$ at Mach 2.5. The increase in fluctuating intensity with the Mach number is consistent with the theory of 'Mach wave radiation' and the experimental findings by Laufer (1964). For both Mach number cases, the pressure fluctuations are strongly correlated with the streamwise velocity (u) and the wall-normal velocity (w), but almost uncorrelated with the spanwise velocity (v). The large negative value of $\overline{u'p'}$ and positive value of $\overline{w'p'}$ indicate that the freestream radiation may be approximated by two-dimensional, backward-facing waves. The changes in values of $\overline{w'p'}/w'_{rms}p'_{rms}$ and $\overline{u'p'}/u'_{rms}p'_{rms}$ between the Mach 2.5 and Mach 5.86 cases indicate a variation of the directionality of the freestream radiation with the Mach number (see section 4.2).

4.2. *Wave-front orientation*

In this section, the directionality of the stochastic acoustic field in the free stream is discussed given its importance to hypersonic transition testing in conventional wind tunnels. Figure 19a shows that the instantaneous pressure field in the free stream consists of randomly spaced wavefronts, each with a limited spatial coherence. The wave fronts exhibit a preferred orientation within the streamwise-wall normal (x-z) plane. The orientation of the instantaneous freestream pressure field is similar to that of the freestream pressure structures that are defined in the statistical sense based on $C_{pp}(\Delta x, z, z_{ref})$ (figure 12d) with $\theta \approx \theta_{xz} = 21°$.

An alternate way of defining the freestream wave-front orientation is to assume that the two-dimensional freestream acoustic field consists of planar acoustic waves. The wave-front orientation can therefore be derived using the following plane-acoustic-wave relation (Liepmann & Roshko 1957)

$$\frac{u'_n}{U_\infty} = \frac{1}{\gamma M_\infty} \frac{p'}{p_\infty} \tag{4.1}$$

where $u_n = \mathbf{u} \cdot \mathbf{n} = u' \cos\theta_n + w' \sin\theta_n$ is the velocity normal to the wave front and $\mathbf{n} = (\cos\theta_n, \sin\theta_n)$ is the plane-wave normal direction with θ_n the angle between $\mathbf{u}$ and $\mathbf{n}$. The wave-front orientation that is statistically most likely can be determined to be the direction that minimizes the difference between $u'_{n,rms}/U_\infty$ and $p'_{rms}/(\gamma M_\infty p_\infty)$. By using the freestream statistics analogous to table 4, $\theta_n \approx 120°$ (correspondingly $\theta \approx 30°$) is obtained. For comparison, the wave angle of acoustic radiation for a Mach 2.5 turbulent boundary layer is $\theta = 42°$ (Duan *et al.* 2014). Laufer (1964) has used a similar but less rigorous relation $u'_n cos\theta_n = u'$ to estimate the wave-orientation, since the streamwise velocity fluctuation u' is the only velocity component that could be measured in his experiments.

The differences in the calculated wave angles θ based on the plane-acoustic-wave assumption and the two-point correlation $C_{pp}(\Delta x, z, z_{ref})$ indicate that the the freestream acoustic field does not correspond to truly planar waves. The deviation from purely planar behavior is also indicated by the imperfect correlation between p' and the streamwise (u') and wall-normal (w')velocity fluctuations in the freestream region (Recall the data presented in table 4). As seen from figure 19b, a substantial portion of the instantaneous pressure field within the region of interest corresponds to conical disturbances propagating from some (possibly virtual) localized source within the boundary layer. The finite spanwise extent of the pressure wavepackets is consistent with the finite size of acoustic sources that are responsible for generating the waves. The details of the acoustic sources will be discussed in section 4.3.

4.3. *Sources of freestream acoustic radiation*

In this section, the acoustic sources that give rise to the acoustic pressure fluctuations in the free stream are approximated in terms of flow turbulence according to the acoustic analogy approach by Phillips (1960). The Phillips' form of the acoustic analogy equation, the definition of acoustic source terms as well as their decomposition into linear and quadratic components are given in Duan *et al.* (2014).

Figure 20a plots the root-mean-square (RMS) of the acoustic source term including both linear and nonlinear components as functions of z across the near-wall portion of the boundary layer. Similar to the Mach 2.5 case (Duan *et al.* 2014), the total source term for the present DNS peaks at $z^+ \approx 20$ and the nonlinear source term is dominant over the linear source term throughout the boundary layer. Among the six constituent terms of the nonlinear acoustic source (figure 20b), $(\partial v'/\partial z)(\partial w'/\partial y)$ has the largest RMS value
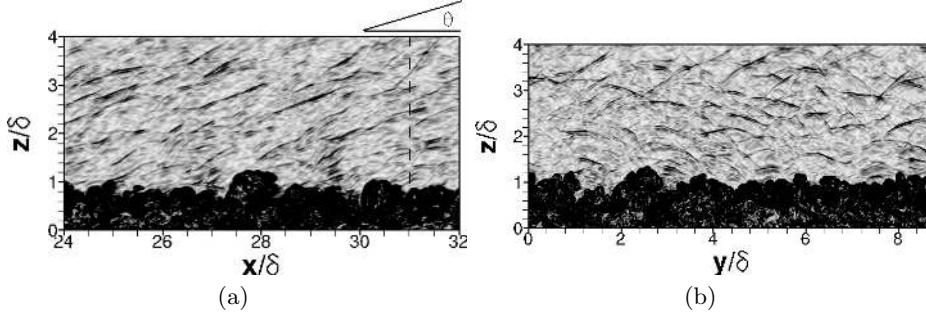
Figure 19: Numerical Schlieren image based on instantaneous flow field for the present DNS of a Mach 5.86 turbulent boundary layer. Contour levels are selected to emphasize disturbances in the freestream. θ is the angle between the flow direction and the acoustic wave front, and the vertical dashed line in (a) indicates the streamwise location of the selected spanwise wall-normal plane visualized in (b).

with approximately the same peak location as the total acoustic source. The dominance of $(\partial v'/\partial z)(\partial w'/\partial y)$ in the buffer layer may indicate the important role played by the near-wall streamwise structures in sound generation. Similar distribution of source terms as well as the dominance of the nonlinear components have been reported by Kim (1989) in the context of incompressible flows.

We note that the magnitude of the source terms is not the sole determinant of the local contribution to the acoustic radiation in the free stream. The solution to the acoustic analogy equation is given by the convolution of the source terms with the Green's function of this equation which may be viewed as the local efficiency of the conversion of hydrodynamic source terms into radiating acoustic disturbances. Due to the dramatic differences in the ability of sound generation between turbulent sources that travel at subsonic or supersonic speeds relative to the frees tream (i.e. the basic concept of 'eddy Mach wave' (Phillips 1960; Ffowcs-Williams & Maidanik 1965)), figure 20a also shows the regions of flow with a supersonic ($M_r > 1$) and subsonic ($M_r < 1$) relative Mach number. The relative sonic location ($M_r = 1$) for the Mach 5.86 lies at $z^+ \approx 114$ ($z/\delta \approx 0.25$), compared with $z^+ \approx 22$ ($z/\delta \approx 0.04$) for the Mach 2.5 case, indicating a dramatic increase in the fraction of sound-radiating eddies as the freestream Mach number increases. The increased portion of sound-generating eddies is consistent with the enhanced radiation intensity as the freestream Mach number increases (figure 7b). Moreover, the increased fraction of the inner layer that can radiate to the free stream contributes to a reduced gap between the peak frequency of fluctuations near the surface and within the free stream as shown by figure 9b.

5. Summary and conclusions

DNS of a zero-pressure-gradient turbulent boundary layer with a nominal freestream Mach number of 5.86 and a wall-to-recovery temperature ratio of $T_w/T_r = 0.76$ is conducted to investigate the wall-normal variation of the fluctuating pressure field and highlight the differences between the primarily vortical pressure signal within the boundary layer and the acoustic pressure signal in the free stream. Computational predictions for both the mean velocity profile and frequency spectrum of surface pressure fluctuations compare well with measurements in a Mach 6 wind tunnel facility, providing what we believe is the first ever comparison of this type at hypersonic Mach numbers. The
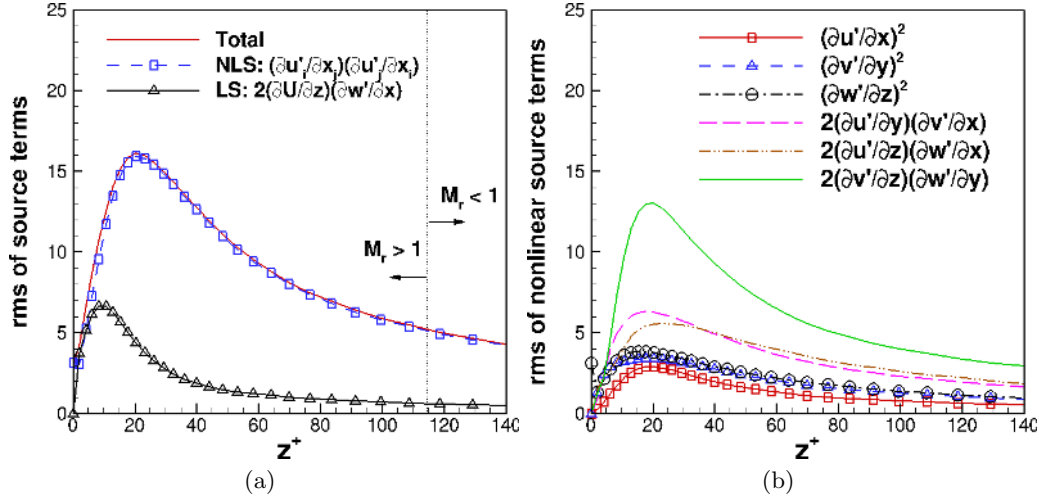
Figure 20: Profiles of the rms source terms (including the total, nonlinear source (NLS), and linear source (LS) terms) across the near-wall portion of the boundary layer. The rms of the source terms are normalized by $\left(\frac{\delta^2}{U_\infty^2}\right)$.

spectrum peak of pressure signals shifts to lower frequencies as the location of interest moves away from the wall. Compared with the pressure signal within the boundary layer, the freestream acoustic pressure fluctuations exhibit a significantly lower dominant frequency, a greater spatial extent, a smaller structure angle, and a smaller bulk propagation speed. Within the boundary layer (except in the immediate vicinity of the wall), Taylor's hypothesis approximately holds with pressure waves propagating with the local mean velocity. In the free stream, however, the propagation speed of pressure fluctuations is significantly smaller than the freestream velocity, even though the 'frozen-eddy' assumption approximately holds as indicated by the value of $\gamma_p \approx 1$ (figure 17). There is an apparent match in the Lagrangian time and spatial scales between the freestream pressure structures and the structures near the wall. Given that the freestream acoustic radiation is generated by turbulent fluctuations within the boundary layer, the apparent match in Lagrangian scales indicates that the acoustic sources are located near the wall. The source terms identified from the standpoint of an acoustic analogy (Phillips 1960) are shown to be located mostly in the buffer layer and dominated by terms that are quadratic in fluctuating velocities. The numerical findings on the acoustic sources are consistent with the theory of 'Mach wave radiation'.

The DNS results are also compared with the recently reported Mach 2.5 DNS (Duan *et al.* 2014) to highlight the variation of acoustic characteristics with Mach number. It is found that the Mach 5.86 DNS exhibits increased radiation intensity, enhanced energy content at high frequencies, shallower orientation of wave fronts with respect to the flow direction, and larger convection velocity relative to the Mach 2.5 case. These variations in the freestream pressure field with Mach number agree well with the experimentally measured trends (Laufer 1964) and are consistent with the 'Mach wave radiation' concept (Phillips 1960; Ffowcs-Williams & Maidanik 1965).

6. Achnowledgments

REFERENCES

BERESH, S. J., HENFLING, J. F., SPILLERS, R. W. & PRUETT, B. O. M. 2011 Fluctuating wall pressures measured beneath a supersonic turbulent boundary layer. *Physics of Fluids* **23** (7).

BERNARDINI, M. & PIROZZOLI, S. 2011 Wall pressure fluctuations beneath supersonic turbulent boundary layers. *Physics of Fluids* **23** (085102).

BERNARDINI, M., PIROZZOLI, S. & GRASSO, F. 2011 The wall pressure signature of transonic shock/boundary layer interaction. *Journal of Fluid Mechanics* **671**, 288–312.

BIES, D. W. 1966 A review of flight and wind tunnel measurements of boundary layer pressure fluctuations and induced structure reponse. *Tech. Rep.*. NASA CR-626.

BLAKE, W. K. 1986 *Mechanics of Flow-Induced Sound and Vibration*. Academic Press, Orlando, Florida.

BOOKEY, P., WYCKHAM, C., SMITS, A. J. & MARTIN, M. P. 2005 New experimental data of stbli at dns/les accessible reynolds numbers. AIAA Paper 2005-309 .

BOUNITCH, A., LEWIS, D. R. & LAFETY, J. F. 2011 Experimental study of second-mode instabilities on a 7-degree cone at Mach 6. In *AIAA Paper 2011-1200*.

BRADSHAW, P. 1967 Inactive motion and pressure fluctuations in turbulent boundary layers. *Journal of Fluid Mechanics* **30**, 241–258.

BULL, M. K. 1996 Wall-pressure fluctuations beneath turbulent boundary layers: Some reflection on forty years of research. *Journal of Sound and Vibration* **190** (3), 299–315.

CADOT, O., DOUADY, S. & COUDER, Y. 1995 Characterization of the low-pressure filaments in a three-dimensional turbulent shear flow. *Physics of Fluids* **7**, 630–646.

CASPER, K. M. 2011 Turbulent pressure fluctuations in a hypersonic boundary layer. AAE 626 Final Project Report, Purdue University, West Lafayette, IN, USA, 2011.

CHOI, H. & MOIN, P. 1990 On the space-time characteristics of wall-pressure fluctuations. *Physics of Fluids* **2** (8), 1450–1460.

DEL ALAMO, J. C. & JIMENEZ, J. 2009 Estimation of turbulent convection velocities and corrections to taylor's approximation. *Journal of Fluid Mechanics* **640**, 5–26.

DOLLING, D. S. & DUSSAUGE, J. P. 1989 A survey of measurements and measuring techniques in rapidly distorted compressible turbulent boundary layers. *AGARDograph* **315**, 1–18.

DONALDSON, J. & COULTER, S. 1995 A review of free-stream flow fluctuation and steady-state flow quality measurements in the AEDC/VKF supersonic tunnel A and hypersonic tunnel B. AIAA Paper 95-6137 .

DUAN, L., BEEKMAN, I. & MARTÍN, M. P. 2010 Direct numerical simulation of hypersonic turbulent boundary layers. part 2: Effect of wall temperature. *Journal of Fluid Mechanics* **655**, 419–445.

DUAN, L., BEEKMAN, I. & MARTÍN, M. P. 2011 Direct numerical simulation of hypersonic turbulent boundary layers. part 3: Effect of Mach number. *Journal of Fluid Mechanics* **672**, 245–267.

DUAN, L., CHOUDHARI, M. M. & WU, M. 2014 Numerical study of pressure fluctuations due to a supersonic turbulent boundary layer. *Journal of Fluid Mechanics* **746**, 165–192.

DUAN, L. & MARTÍN, M. P. 2011 Direct numerical simulation of hypersonic turbulent boundary layers. part 4: Effect of high enthalpy. *Journal of Fluid Mechanics* **684**, 25–59.

ELÉNA, M. & LACHARME, J. P. 1988 Experimental study of a supersonic turbulent boundary layer using a laser doppler anemometer. *Journal de Mécanique Théorique et Appliquée* **7** (2), 175.

FFOWCS-WILLIAMS, J. E. & MAIDANIK, G. 1965 The Mach wave field radiated by supersonic turbulent shear flows. *Journal of Fluid Mechanics* **21**, 641–657.

GANAPATHISUBRAMANI, B., CLEMENS, N., HAMBLETON, W. T., LONGMIRE, E. K. & MARUSIC, I. 2005 Investigation of large-scale coherence in a turbulent boundary layer uisng two-point correlations. *Journal of Fluid Mechanics* **524**, 57–80.

GANAPATHISUBRAMANI, B., CLEMENS, N. T. & DOLLING, D. S. 2006 Large-scale motions in a supersonic turbulent boundary layer. *Journal of Fluid Mechanics* **556**, 271–282.

GLOERFELT, X. & BERLAND, J. 2013 Turbulent boundary-layer noise: Direct radiation at mach number 0.5. *Journal of Fluid Mechanics* **723**, 318–351.

GUARINI, S. E., MOSER, R. D., SHARIFF, K. & WRAY, A. 2000 Direct numerical simulation of a supersonic turbulent boundary layer at Mach 2.5. *Journal of Fluid Mechanics* **414**, 1–33.

HARRIS, J. & BLANCHARD, D. 1982 Computer program for solving laminar, transitional, or turbulent compressible boundary-layer equations for two-dimensional and axisymmetric flow. NASA-TM-83207 .

JIANG, G. S. & SHU, C. W. 1996 Efficient implementation of weighted ENO schemes. *Journal of Computational Physics* **126** (1), 202–228.

KAT, R. DE & OUDHEUSDEN, B. W. VAN 2012 Instantaneous planar pressure determination from PIV in turbulent flows. *Experiments in Fluids* **52** (5), 1089–1106.

KENDALL, J. M. 1970 Supersonic boundary layer transition studies. *Space Program Summary* **3**, 43–47.

KIDA, S. & MIURA, H. 1998 Identification and analysis of vortical structures. *European Journal of Mechanics - B/Fluids* **17** (4), 471–488.

KIM, J. 1989 On the structure of pressure fluctuations in simulated turbulent channel flow. *Journal of Fluid Mechanics* **205**, 421–451.

KIM, J. & HUSSAIN, F. 1993 Propagation velocity of perturbations in turbulent channel flow. *Physics of Fluids* **5** (3), 695–706.

KIM, K. C. & ADRIAN, R. J. 1999 Very large-scale motion in the outer layer. *Physics of Fluids* **11**, 417–422.

KISTLER, A. L. & CHEN, W. S. 1963 The fluctuating pressure field in a supersonic turbulent boundary layer. *Journal of Fluid Mechanics* **16**, 41–64.

KOVASZNAY, L. S. G. 1953 Turbulence in supersonic flow. *Journal of Aeronautical Sciences* **20**, 657–674.

LAUFER, J. 1964 Some statistical properties of the pressure field radiated by a turbulent boundary layer. *Physics of Fluids* **7** (8), 1191–1197.

LIEPMANN, H. W. & ROSHKO, A. 1957 *Elements of Gasdynamics*. John Wiley & Sons, Inc. New York.

MAESTRELLO, L. 1969 Radiation from and panel response to a supersonic turbulent boundary layer. *Journal of Sound Vibration* **10** (2), 261–262.

MARCO, A. DI, CAMUSSI, R., BERNARDINI, M. & PIROZZOLI, S. 2013 Wall pressure coherence in supersonic turbulent boundary layers. *Journal of Fluid Mechanics* **732**, 445–456.

MARTÍN, M.P. 2007 DNS of hypersonic turbulent boundary layers. part i: Initialization and comparison with experiments. *Journal of Fluid Mechanics* **570**, 347–364.

MASUTTI, M., CHAZOT, E. & CARBONARO, M. 2012 Disturbance level characterization of a hypersonic blowdown facility. *AIAA Journal* **50** (12).

MORGAN, B., LARSSON, J., KAWAI, S. & LELE, S. K. 2011 Improving low-frequency characteristics of recycling/rescaling inflow turbulence generation. *AIAA Journal* **49** (3), 582–597.

NAKA, Y., STANISLAS, M., FOUCAUT, J. M., COUDERT, S., LAVAL, J. P. & OBI, S. 2015 Space-time pressure-velocity correlations in a turbulent boundary layer. *Journal of Fluid Mechanics* **771**, 624–675.

PATE, S. R. 1978 Dominance of radiated aerodynamic noise on boundary-layer transition in supersonic-hypersonic wind tunnels. *Tech. Rep.* AEDC-TR-77-107. Arnold Engineering Development Center.

PELTIER, S. J., HUMBLE, R. A. & BOWERSOX, R. D. W. 2012 PIV of a mach 5 turbulent boundary layer over diamond roughness elements. AIAA Paper 2012-3061 .

PHILLIPS, O. M. 1960 On the generation of sound by supersonic turbulent shear layers. *Journal of Fluid Mechanics* **9**, 1–28.

PIPONNIAU, S., DUSSAUGE, J. P., DEBIEVE, J. F. & DUPONT, P. 2009 A simple model for low-frequency unsteadiness in shock-induced separation. *Journal of Fluid Mechanics* **629**, 87–108.

PIROZZOLI, S. & BERNARDINI, M. 2011 Turbulence in supersonic boundary layers at moderate Reynolds numbers. *Journal of Fluid Mechanics* **688**, 120–168.

PRIEBE, S. & MARTÍN, M. P. 2012 Low-frequency unsteadiness in shock wave-turbulent boundary layer interaction. *Journal of Fluid Mechanics* **699**, 1–49.

SCHLATTER, PHILIPP & ÖRLÜ, RAMIS 2010 Assessment of direct numerical simulation data of turbulent boundary layers. *Journal of Fluid Mechanics* **659**, 116–126.

SCHNEIDER, S. P. 2001 Effects of high-speed tunnel noise on laminar-turbulent transition. *Journal of Spacecraft and Rockets* **38** (3), 323–333.

SCHNEIDER, S. P. 2008 Development of hypersonic quiet tunnels. *Journal of Spacecraft and Rockets* **45** (4), 641–664.

SIMENS, M. P., JIMENEZ, J., HOYAS, S. & MIZUNO, Y. 2009 A high-resolution code for turbulent boundary layers. *Journal of Computational Physics* **228** (11), 4218–4231.

SMITS, A. J. & DUSSAUGE, J. P. 2006 *Turbulent Shear Layers in Supersonic Flow*, 2nd edn. American Institute of Physics.

SPALART, P. R. 1988 Direct simulation of a turbulent boundary layer up to $re_\theta = 1410$. *Journal of Fluid Mechanics* **187**, 61–98.

STAINBACK, P. C. 1971 Hypersonic boundary-layer transition in the presence of wind tunnel noise. *AIAA Journal* **9** (12), 2475–2476.

STEEN, L. E. 2010 Characterization and development of nozzles for a hypersonic quiet wind tunnel. Master's thesis, Purdue University, West Lafayette, IN, USA.

TAYLOR, E. M., WU, M. & MARTÍN, M. P 2006 Optimization of nonlinear error sources for weighted non-oscillatory methods in direct numerical simulations of compressible turbulence. *Journal of Computational Physics* **223** (1), 384–397.

THOMPSON, KEVIN W. 1987 Time dependent boundary conditions for hyperbolic systems. *Journal of Computational Physics* **68** (1), 1–24.

TOMKINS, C. D. & ADRIAN, R. J. 2003 Spanwise structure and scale growth in turbulent boundary layers. *Journal of Fluid Mechanics* **490**, 37–74.

TSUJI, Y., FRANSSON, J. H. M., ALFERDSSON, P. H. & JOHANSSON, A. V. 2007 Pressure statistics and their scaling in high-reynolds-number turbulent boundary layers. *Journal of Fluid Mechanics* **585**, 1–40.

TSUJI, Y., IMAYAMA, S., SCHLATTER, P., ALFREDSSON, P. H., JOHANSSON, A. V., MARUSIC, I., HUTCHINS, N. & MONTY, J. 2012 Pressure fluctuation in high-reynolds-number turbulent boundary layer: Results from experiments and dns. *Journal of Turbulence* **13** (50), 1–19.

WELCH, P. D. 1967 The use of fast fourier transform for the estimation of power spectra: A method based on time averaging over short, modified periodograms. *IEEE Trans. Audio Electroacoustics* **AU-15**, 70–73.

WILLIAMSON, J.H. 1980 Low-storage runge-kutta schemes. *Journal of Computational Physics* **35** (1), 48–56.

WILLMARTH, W. W. 1975 Wall pressure fluctuations beneath turbulent boundary layers. *Annual Review of Fluid Mechanics* **7**, 13–36.

WU, M. & MARTÍN, M. P 2007 Direct numerical simulation of supersonic boundary layer over a compression ramp. *AIAA Journal* **45** (4), 879–889.

WU, M. & MARTÍN, M. P. 2008 Analysis of shock motion in shockwave and turbulent boundary layer interaction using direct numerical simulation data. *Journal of Fluid Mechanics* **594**, 71–83.

XU, S. & MARTÍN, M. P. 2004 Assessment of inflow boundary conditions for compressible turbulent boundary layers. *Physics of Fluids* **16** (7), 2623–2639.